ELSEVIER

Contents lists available at ScienceDirect

Materials Science & Engineering A

journal homepage: www.elsevier.com/locate/msea



Energy- and material-efficient Ti-6Al-4V sheet part fabrication by the novel TISTRAQ-process, including resistance heating and tool-based quenching: Insights into test stand design and material potential

Nina Pfeffer ^{a,*,1}, Maximilian Alexander Kaiser ^{b,1}, Werner Feix ^c, Nils Kälble ^d, Mathias Merten ^c, Andreas Stark ^e, Andre Haufe ^c, Thomas Meyer ^d, Thomas Tröster ^b, Heinz Werner Höppel ^a

ARTICLE INFO

Keywords: Test stand design Ti-6Al-4V Resistance heating Tool-based quenching Non-isothermal hot forming Material-efficiency Energy-efficiency Microstructures Martensite Annealing Strengthening

ABSTRACT

Sustainable and lightweight manufacturing processes are essential for reducing greenhouse gas emissions and conserving resources. The novel TISTRAQ-process combines a two-stage, short-time heat treatment with an advanced heating and non-isothermal hot forming strategy, thereby ensuring high material and energy efficiency. In this work, a simplified laboratory-scale test stand was developed, enabling direct electric resistance heating and subsequent tool-based quenching of Ti-6Al-4V sheet strips under near-process conditions, but without the complexity of simultaneous forming. The setup allows systematic variation of key process parameters with minimal material consumption, an approach applied in this study to investigate their influence on material properties. Finite element simulations supported the test stand design and provided a valuable understanding of temperature inhomogeneities and their relevance for microstructural evolution and process control. The paper provides detailed insights into (i) the design and capabilities of the test stand, (ii) simulation-based evaluation of temperature homogeneity, (iii) the TISTRAQ process route - including resistance heating, tool-based quenching, and additional short-time annealing, (iv) the resulting microstructural and mechanical properties, and (v) the material response to critical parameters. Experimental results confirm the high potential of the TISTRAQ-process to enhance the tensile strength of Ti-6Al-4V. The solution heat treatment temperature and time delay prior to quenching were identified as critical parameters due to their strong influence on microstructure and mechanical behavior. Overall, the study demonstrates how tailored process control can unlock the material potential of Ti-6Al-4V. It also indicates a good scalability of the TISTRAQ-process for lightweight, resource-efficient production of next-generation titanium alloy sheet parts.

1. Introduction

TISTRAQ-Process

Ti-6Al-4V is one of the most widely used titanium alloys in the aerospace industry, due to its balanced properties such as high specific strength, adequate fatigue strength and excellent corrosion resistance. Its application as thin-walled sheet metal components is also of high interest. However, the forming process requires special measures, often

resulting in long processing times and high costs. The main cost drivers are the high energy consumption and measures for oxidation prevention when hot forming comes into play. The hexagonal crystal structure of the two-phase titanium alloy Ti-6Al-4V results in limited formability, significant anisotropy of the mechanical properties and pronounced tensile-compressive asymmetry, also known as Bauschinger effect [1,2]. Sheet metal parts made of titanium alloys exhibit a strong springback

^a Friedrich-Alexander-Universität Erlangen-Nürnberg (FAU), Department of Materials Science & Engineering, Institute I: General Materials Properties, Erlangen, Germany

b Paderborn University, Faculty of Mechanical Engineering, Institute for Lightweight Design with Hybrid Systems, Chair of Automotive Lightweight Design (LiA), Paderborn, Germany

^c Dynamore GmbH, an Ansys Company, Stuttgart, Germany

^d HEGGEMANN AG, Büren, Germany

^e Helmholtz-Zentrum Hereon, Geesthacht, Germany

 $^{^{\}star}$ Corresponding author.

E-mail address: nina.pfeffer@fau.de (N. Pfeffer).

¹ these authors contributed equally to this work.

behavior, which is due to the high elastic energy absorption of the material and leads to deviations in terms of dimensional accuracy [3,4]. Therefore, extending the forming limits of titanium alloys is crucial for the effective production of thin-walled sheet metal parts. Hot forming offers great potential in this respect [5]. While isothermal hot forming is used for simple components, superplastic forming using gas pressure is suitable for more complex components [6–9]. Kopec et al. [10] observed an anomalous increase in ductility of Ti-6Al-4V in the isothermal hot tensile test with increasing temperature starting from 700 °C. At lower strain rates and a temperature of 750 °C the material exhibited superplastic material behavior in the investigations by Salishchev et al. [11]. Britton et al. [12] attribute the increased ductility at higher temperatures to the activation of additional slip systems with respect to the pyramidal plane. The studies conducted by Chen et al. [13] and Zong et al. [14] demonstrate that springback is substantially reduced by the process of hot forming. The drawbacks associated with isothermal hot forming include the necessity for an additional protective gas atmosphere, the long process times that are concomitant with increased exposure times and α -case formation, the high energy consumption and the substantial thermal wear of the tools [2].

Non-isothermal hot forming processes have been developed to counteract the disadvantages associated with isothermal hot forming, thereby enabling more efficient forming of titanium alloys. In contrast to isothermal hot forming, only the sheet metal is heated to the forming temperature, while the tools remain at room temperature [15].

Due to the rapid cooling rate of sheet metal during the forming process, relatively high transfer and forming speeds are necessary [16]. In the research conducted by Odenberger et al. [15] and Kopec et al. [10], a blank was initially heated in a furnace, subsequently transferred to a forming tool and successfully formed. Hamedon et al. [17] investigated the effects of resistance heating on the process of forming and found that it not only improved formability, but also established a direct correlation between springback behavior and preheating temperature. Building upon these findings, Ozturk et al. [18] utilized an identical test setup at 900 °C, thereby achieving a complete suppression of springback. In another study by Ozturk et al. [19] the advanced industrial potential of non-isothermal hot forming on a 550 mm long demonstrator part using resistance heating has been demonstrated.

It is evident that a combination of heat treatment and non-isothermal hot forming, as it is the case with press-hardening of steel or hot forming of aluminum, can yield a notable enhancement in efficiency [20–22]. For press-hardening, a steel-sheet undergoes austenitization, followed by quench-forming using water-cooled tools. The cooling rates achieved in this process are comparable to those of water quenching [16].

In previous work, Pfeffer et al. [23] solution heat treated Ti-6Al-4V sheet material in the upper $\alpha+\beta$ two phase region and subsequently quenched it in water. The resulting $\alpha+\alpha'$ -microstructures in this alloy system are a customary outcome when high cooling rates above a critical value are implicated by which a non-diffusional martensitic transformation ($\beta \rightarrow \alpha'$) is caused. Consequently, such $\alpha + \alpha'$ -microstructures are also expected after non-isothermal forming in water-cooled tools. These microstructures are characterized by a lower yield strength, a similar ultimate strength, but significantly better work hardening behavior and improved ductility compared to the as-received rolled and mill annealed material [23]. Similar findings have also been described in other works, that have been carried out on Ti-6Al-4V alloy, but not on thin sheet material [24-27]. Accordingly, the martensite in the Ti-6Al-4V $\alpha + \alpha'$ -microstructures does not have a direct hardening effect, in contrast to the martensite in carbon-containing steels, in which interstitial C-atoms evoke an increased hardness due to a distortion of the martensitic lattice structure [28-30]. However, in previous work by Pfeffer et al. [23], a significant increase in strength of the Ti-6Al-4V sheet material was achieved by an additional short-time annealing at 570 °C for 180 s, followed by air cooling, subsequently to the solution heat treatment and quenching step. This increase was attributed to nano-scale microstructural changes within in the martensitic

transformed prior β -phase, most likely reflecting an initial stage of martensite decomposition. Further results from the literature on Ti-6Al-4V also indicate a potential for increasing strength through subsequent annealing of $\alpha+\alpha'$ microstructures [31–34].

In light of the extant literature and bringing their main findings together, our primary objective is to develop an energy-efficient process for the production of Ti-6Al-4V sheet parts that makes efficient use of the Ti-6Al-4V sheet material and maximizes its potential. This process, denoted as "TISTRAQ"-process, will involve two steps:

- Direct electric resistance heating, short-time holding at target solution heat treatment temperature and rapid quench-forming (or even only quenching) by means of water-cooled tools.
- Subsequent short-time annealing in a furnace in order to specifically influence the material properties.

An additional post-processing surface treatment step may be necessary for applications requiring compliance with specific standards. Notably, for aerospace components, such treatments are mandated.

This work had several objectives, which are subordinate to the main objective. One primary goal was to develop a simplified laboratory-scale test stand at HEGGEMANN AG based on the TISTRAQ-process, but initially disregarding the forming. This test stand was aimed at facilitating direct resistance heating of sheet metal strips and subsequent quenching of the strips using water-cooled tools. By this it was sought to enable a systematic evaluation of the influence of TISTRAQ-specific process parameters with only a moderate material consumption. The simplified consideration without the forming was deliberately chosen to avoid the interaction of different effects and thus ensure the isolation of specific process parameters. In order to gain information on the homogeneity of temperature in the resistance heated Ti-6Al-4V sheet strip, a further goal was a finite element simulation of the temperature field. Therefore, the Ansys LS-DYNA® software [35] was utilized and material properties from literature used as input-values. Lastly, the utilization of the developed test stand was intended to achieve two primary objectives: firstly, to demonstrate the material potential of the Ti-6Al-4V alloy through the TISTRAQ-process, and secondly, to evaluate the influence of TISTRAQ-specific process parameters on the microstructure and mechanical properties of Ti-6Al-4V sheet material, with the latter also identifying critical process variables. To this end, a set of promising parameters for TISTRAQ-related processing was defined based on material-scientific preliminary tests conducted at the Institute I of FAU as partially published in Ref. [23] and in alternative literature. This standard parameter set was utilized as a base from which specific parameters were systematically varied. The general material evolution along the processing chain as well as the effect of two critical parameters: (i) solution heat treatment temperature and (ii) time-delayed quenching are addressed in the results section of this paper. The produced resistance heated and tool quenched (RHTQ) material states were characterized. The same was done after an additional annealing at 570 °C for 180 s, which was performed in a vertical furnace. The evaluation of the microstructure was facilitated by the use of scanning electron microscopy (SEM) and high-resolution X-ray diffraction (HRXRD). The mechanical properties were characterized by means of hardness and tensile tests.

Some aspects of the present study have already been addressed in the conference papers [36,37]. However, this paper builds upon those works by providing a more in-depth analysis in selected areas, introducing additional topics, and offering a broader and more holistic perspective on the major topic.

2. Experimental setup and methodology

2.1. Development of a laboratory-scale test stand and sample production

A dedicated test stand was developed comprising a resistance

heating unit for solution heat treatment and a quenching unit for toolbased quenching of the Ti-6Al-4V alloy specimen. Both system components are connected to each other via a linear guide and build the toolbased heat treatment test stand, as depicted in Fig. 1. The test stand is controlled using *LabVIEW* from *National Instruments*. A comprehensive description of the design and the testing procedure is provided in Section 3.1.

The specimen geometry for heat treatment in the tool-based heat treatment test stand is shown in Fig. 2. The specimen is 163 mm long with a heating length of 123 mm. The standard specimen width is 11 mm. In addition, specimen widths from 6 mm to 40 mm can be used to cover a wider range of achievable surface pressures. The two 4.5 mm holes, compare Fig. 2, are used to position and fasten the specimens to the copper clamps of the heating unit. The samples are cut from the sheet metal using a 2D laser cutter, deburred and then cleaned with ethanol. A hole of 0.6 mm diameter and 2.5 mm depth is drilled in the center of the sample to measure and control the sample temperature.

2.2. Definition of the simulation model

The simulation results presented in Section 3.2 were obtained using the finite element (FE) LS-DYNA software. A key advantage of LS-DYNA is its capacity to serve as a versatile, finite element system incorporating explicit and implicit time integration schemes, thereby enabling the modeling of the targeted multi-physics problems within a single simulation model. This capability is a consequence of the coupling of the electromagnetic (EM) solver with the thermal solver and the mechanical solver.

To simulate the test stand, a FE-model of the specimen was designed, incorporating boundary conditions, compare Fig. 3, and material properties. The mechanical, electrical and thermal material properties employed as input values for the simulation of the titanium alloy were partially derived from calculations executed with the <code>JMatPro®</code> software [38] in previous studies conducted by Kaiser et al. [36] and partially sourced from the <code>VDI Heat Atlas</code> [39]. In order to ensure the accuracy of the calculation of the temperature gradient within the Ti-6Al-4V sheet strip, the solid model was meshed with an element size of 0.5 mm. Additionally, in order to model the geometric resolution of the drill hole with a sufficiently high accuracy, a smaller element size of approximately 0.15 mm was chosen in the area of the drill hole.

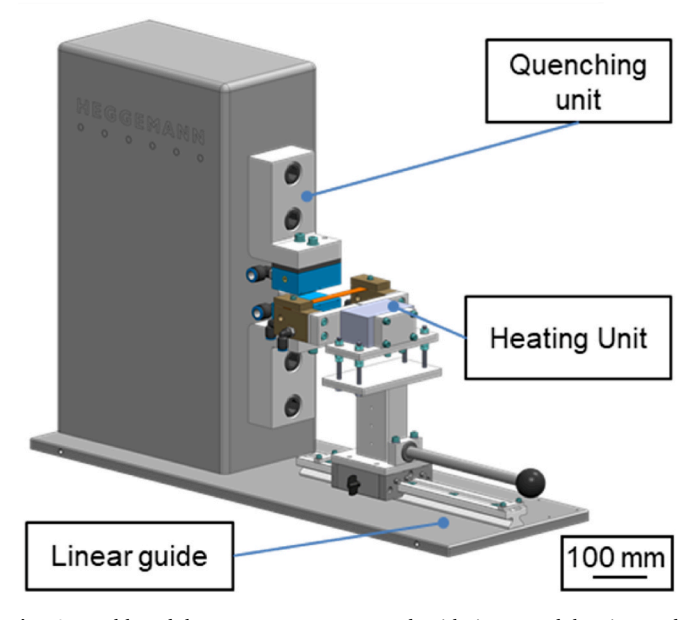


Fig. 1. Tool-based heat treatment test stand with integrated heating and quenching unit for solution heat treatment and quenching on a laboratory scale.

Furthermore, the peripheral zones between the drill hole and the outer skin were meshed with three elements and an element edge length of approximately 0.08 mm instead of one single element. This resulted in an improved resolution of the temperature gradient.

In the simulation, an initial ambient temperature of 25 °C was set using the *INITIAL_TEMPERATURE_SET keyword. In order to describe the cooling of the copper clamps at the edge regions of the specimen in the FE model, shown in red in Fig. 3, the outer segments of the edge regions were subjected to a convection boundary condition with respect to 25 °C and a constant heat transfer coefficient. The outer segments of the center sample area that were not covered or unaffected by copper clamps but instead only affected by the ambient atmosphere are depicted in brown in Fig. 3. These segments were provided with convection and radiation boundary conditions relative to calm air at 25 °C.

In order to model resistance heating, isopotentials were defined, at the points of contact between the copper clamps and the specimen, using the keyword *EM_ISOPOTENTIAL. The use of the keyword *EM_ISOPOTENTIAL_CONNECT enabled the connection of the two isopotentials, thus allowing for the specification of various electrical boundary conditions, such as voltage, electric current and resistance [40]. In the present case, the electric current was specified with the objective of achieving a target temperature of 915 °C at the bottom of the drill hole.

In the experimental setup described in Section 2.1, a hole with as depth of 2.5 mm a diameter of 0.6 mm is equipped with a thermocouple (TC) to measure the temperature in the metal strip. The thermocouple was not modeled in the simulation since the temperatures can be post-processed directly at the nodes. To account for the thermal mass of the thermocouple, an additional convection boundary condition for the hole was added. Since no convection is expected within the drill hole containing the thermocouple, all surfaces of the drill hole were excluded from the convection boundary condition.

2.3. Material characterization

2.3.1. Overview of material states taken into account

The initial Ti-6Al-4V Grade 5 sheet material with a thickness of 1 mm was purchased from Lasting Titanium and was received in a rolled and mill-annealed condition. Its chemical composition lies within the specified limits in AMS 4911 (for detailed composition, see Ref. [23]). Ti-6Al-4V material states were produced by resistance heating and tool-based quenching (RHTQ) in the developed laboratory-scale test stand. Specifically, the pure RHTQ samples are indicative of a specific heat treatment process involving solution heat treatment, followed by quenching (STQ). Table 1 provides an overview of the experimental series performed and the corresponding RHTQ-STQ conditions produced. To minimize the influence of material and experimental procedure and clearly isolate the effect of the process parameters (e.g., $T_{\rm ST}$ or $t_{\rm QD}$), sheet strips were taken from comparable areas of the AR sheet material, and the same thermocouple was used within one experimental series.

All produced RHTQ-STQ material states were characterized both in the RHTQ-STQ state and after an additional short-time annealing at 570 °C for 180 s. The annealing treatment was performed in a *THERM-CONCEPT ROC* 105/610/15 vertical furnace according to the procedure described in Ref. [23] for the short-time annealing step. The solution heat treated and additionally annealed samples (STA) are hereafter referred to as RHTQ-STA.

2.3.2. Sampling and sample preparation

Three specimens were taken from the core of one sheet metal strip for microstructural analysis and hardness testing. The specimens were marked with letters according to the orientation of the drilled hole pointing upwards, as shown in Fig. 4: a) to the left of the hole, b) center, c) to the right of the hole.

Sample a) was used for hardness testing, sample b) for scanning

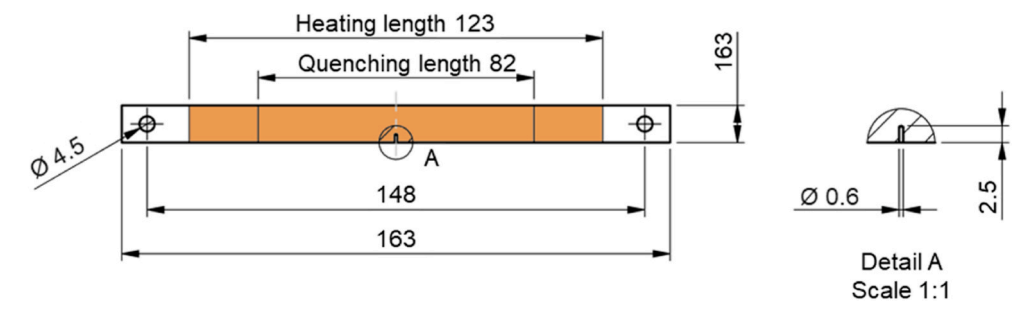


Fig. 2. Specimen geometry for tool-based heat treatment (orange area indicates heating range). (For interpretation of the references to colour in this figure legend, the reader is referred to the Web version of this article.)

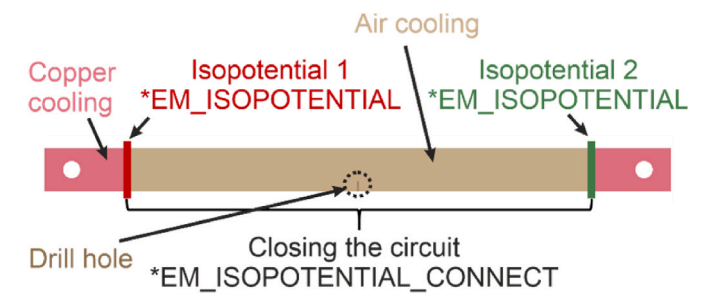


Fig. 3. Schematic depiction of the FE-Model for the resistance heated sheet strip with the boundary conditions applied.

Table 1Matrix providing an overview of the standard RHTQ-STQ condition, the varied RHTQ parameters as well as the variations.

Standard STQ condition produced by means of RHTQ: heating rate 60 K/s, nominal solution heat treatment temperature 915 $^{\circ}$ C. solution heat treatment time 60 s, closing velocity 21 mm/s, contact pressure 10 MPa, quenching delay time 0 s

Varied Parameter	Variations		
Solution heat treatment temperature T _{ST}	875 °C, 895 °C, 915 °C, 935 °C		
(nominal) Quenching delay time t _{OD}	0 s, 2 s, 4 s, 6 s		

electron microscopy (SEM) microstructural analysis, and sample c) for high energy X-ray diffraction (HEXRD) microstructural characterization of the respective sheet metal strip. The transverse direction (TD) of the sheet was chosen as the observation and testing direction for samples of type a) and b). The specimens for the hardness testing and SEM analysis were embedded with the opposite side of the hole facing down and prepared by wet grinding with SiC abrasive paper in several steps, starting with 320 grit and ending with 4000 grit, and ensuring plane-parallelism. It was further ensured that approximately 2 mm in TD

towards the site of investigation was removed in all cases in order to ensure consistency and thus comparability between the different material states. The SEM samples underwent an additional polishing procedure. The first polishing step consisted of a 3 μm diamond suspension at a force of 20 N for 10 min. The final step was a chemo-mechanical polish with a SiO $_2$ oxide polishing (OPS, from Schmitz Metallographie GmbH) suspension to which a small amount of $\rm H_2O_2$ (9:1 ratio) had been added, at 15 N for 15 min. In contrast to samples a) and b) no further preparation was applied for the samples used for HEXRD experiments after cutting.

For tensile specimen production, four sheet metal strips per material state were produced on the test stand using identical process parameters. Tensile specimens with the geometry shown in Fig. 4 d) were then machined from the sheet metal strips. This geometry fits to the geometrical specifications for samples from flat products of thickness 0.1–3.0 mm given in DIN 50125.

2.3.3. Microstructural characterization and mechanical testing

On one hand microstructural analysis was conducted utilizing a *Zeiss Crossbeam* 540 EsB SEM equipped with a *Zeiss 4QBSD* backscattered electron (BSE) detector. The SEM-BSE analysis was performed on microstructural samples (preparation compare Section 2.3.2) with the following parameters: an acceleration voltage of 10 kV, a probe current of 5 nA, and a working distance of 8.5 mm. In this manner, microstructural images were generated both from the interior and from the near-surface regions of the samples, thereby illustrating microstructural characteristics on the micro- and coarser nanoscale. The secondary electron (SE) contrast and the identical parameters as listed above were used to facilitate the visualization of oxides.

In order to reveal microstructural changes at the fine nanoscale level, some of which are not visible in the SEM, HEXRD was used as an additional method. The HEXRD experiments were conducted at the Hamburg-based *DESY* facility, employing the Hereon-operated beamline *P07: High Energy Materials Science beamline*. Ex situ measurements on the HEXRD sheet samples (compare Section 2.3.2 for sampling) were conducted at an X-ray energy of 103.3 keV ($\lambda = 0.120$ Å) and with a beam

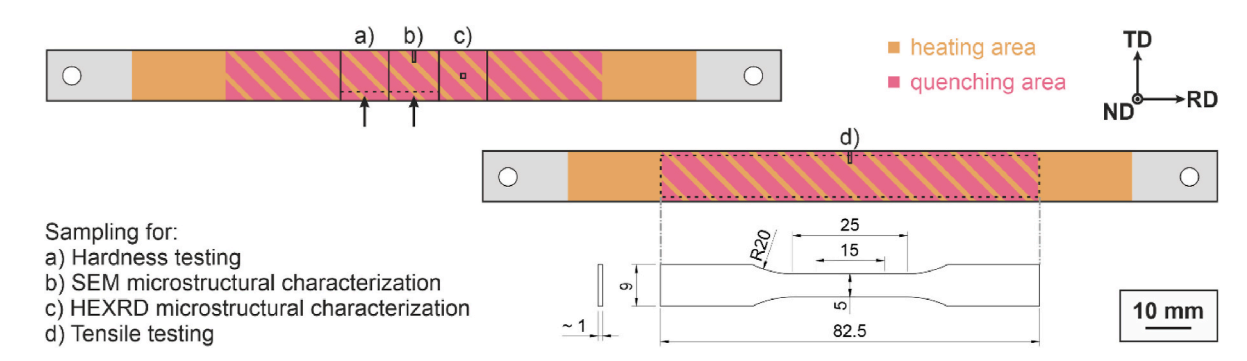


Fig. 4. Sampling from the RHTQ Ti-6Al-4V sheet strips: specimens for a) hardness testing in TD, b) SEM investigation in TD, c) HEXRD experiments and d) tensile testing.

spot size of 1 mm \times 1 mm. The samples were irradiated in the normal direction with the beam spot aligned to the sample center. To enhance the quality of grain statistics, the samples were additionally rotated $\pm 10^{\circ}$ around the rolling direction axis. The distance between the sample and the detector was 1630 mm, and the diffraction rings were recorded using a <code>PerkinElmer XRD 1621</code> area detector with a pixel size of 200 μ m \times 200 μ m.

An oxygen content analysis was conducted via carrier gas hot extraction (CGHE) on a *Leco TCH600* instrument in accordance with ASTM E-1409. This analysis was conducted on the as-received material and a resistance heated and tool quenched condition (with both oxide and oxide removal). The oxygen content was measured throughout the entire sample volume of cuboids measuring $\sim 3.8 \times 3.8 \times 1$ mm, which were cut out of sheet strips using a wire saw. Per material state, three cuboids were measured. The defined surface-to-volume ratio made it possible to compare the oxygen content between the three conditions and to estimate the oxygen absorption from the ambient atmosphere during processing.

Macrohardness testing was carried out using a *KBW 10-V* Vickers hardness tester of the company *KW Prüftechnik*. The Vickers hardness was determined by indenting with a load of 5 kp (HV5) in the TD of the hardness samples (preparation compare Section 2.3.2), and the mean value was calculated by taking five indents per material state and averaging them.

Tensile testing was performed to gain further information about the deformation behavior of different material states. An *Instron 4505* universal testing machine equipped with a Hegewald & Peschke control system was utilized and tensile samples of the geometry shown above were tested with an engineering strain rate of 10^{-3} 1/s according to DIN EN ISO 6892-1. The force was measured by a 20 kN load cell and the displacement by a *laserextensometer* from *Fiedler Optoelektronik GmbH*. Per material state, four tests were performed to guarantee statistics. The mean characteristic values were built from at least three valuable tests (N \geq 3).

3. Results and discussion

3.1. Process design and energy efficiency

The laboratory-scale test stand for resistance heating and tool-based quenching is shown in Fig. 5 before and during solution heat treatment. The Ti-6Al-4V sheet strip is resistance heated and solution heat treated in the heating unit. This is followed by tool-based quenching in the quench unit by direct heat transfer from the titanium sheet material to the punches.

The heating unit is based on direct resistance heating, whereby heat is generated in a current-carrying conductor with a resistor according to Joule's law. The sample is clamped between two water-cooled copper clamps connected by copper wires to an AC transformer. In this way, temperatures more than 1200 $^{\circ}$ C can be achieved at heating rates of up to 60 K/s. A thermal compensation unit is installed to compensate for

thermal expansion and to prevent buckling of the specimen during heating. The applied tensile load is only 100 N to avoid plastic prestraining of the material at elevated temperatures. Four individual threaded spindles are installed below the compensation unit for vertical adjustment of the specimen position. A linear guide, on which the heating unit is positioned, allows precise feeding of the specimen into the quenching unit so that the specimen is quenched tool-based. Multiple insulators are installed at critical points to prevent short circuits.

The quenching unit is composed of a press with pneumatic synchronous kinematics, which introduces force into two water-cooled punches via stiffness-optimized brackets. In consideration of the geometric constraints inherent to the kinematics, both sides of the punch are moved towards each other synchronously. Consequently, the Ti-6Al-4V specimen is contacted and quenched simultaneously on both sides. The applied force ranges from 1.5 to 9.75 kN, with the option to varying the pressure via the specimen width.

The punches are made of hardened Cr7V-L hot-working tool steel, with a hardness of 55 HRC to avoid excessive tool wear and to ensure good thermal conductivity. The contact surface measures 82×50 mm, with a thickness of 30 mm (see Fig. 6 a)). The integration of tool cooling is a crucial aspect of the testing series, as it prevents the punches from overheating and enables efficient heat treatment. The cooling of the punches is facilitated by a circulation cooling unit and integrated cooling channels with a diameter of 9 mm, which are located 12.5 mm below the surface. The design of the cooling channels has been simulated with *LS-DYNA* to ensure that there is no direct influence of the punch cooling on the cooling behavior of the sample, thus ensuring the integrity of the test. The punch temperatures are measured using a 2 mm NiCr-Ni thermocouple (type K – class 1) with a grounded measuring tip. To this end, a hole with a diameter of 2.1 mm and a depth of 25 mm was drilled 2 mm below the surface of the punch (see Fig. 6 a)).

The use of rubber-based buffer elements with a hardness of 65 ± 5 Shore A between the punches and the brackets compensates for manufacturing tolerances in the quenching unit and facilitates uniform contact with the specimen, as shown in the measurements using pressure measuring foil in Fig. 6 b). This is essential to ensure uniform cooling of the specimen.

The surface of the punches has been ground to achieve a high degree of flatness and surface quality (see Fig. 6 c). As shown in Fig. 6 d), a 4.5 \times 2.5 mm section of the ground punch surface was measured using a 3D profilometer (VR3200, Keyence) with a white light strip projection. The resultant average roughness depth, R_z , was determined to be 3.64 \pm 0.69 μm . It is evident that the grinding process has yielded a surface that is particularly even and homogeneous, with only minor residual unevenness. Due to this, a uniform and high heat transfer between the rolled Ti-6Al-4V surface and the punches can be achieved [16].

The measurement and control of the sample temperature is achieved as follows: Drilling a hole in the center of the sample with a diameter of 0.6 mm and a depth of 2.5 mm and positioning a NiCrSi-NiSi thermocouple (type N - class 1) with an insulated measuring tip and a diameter of 0.5 mm in it. The thermocouple is affixed in the drill hole and a

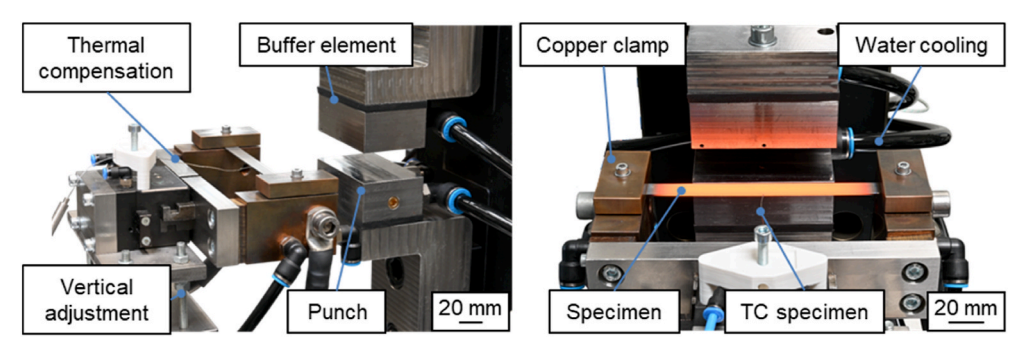


Fig. 5. Tool-based heat treatment test stand with integrated heating and quenching unit for solution heat treatment and quenching.

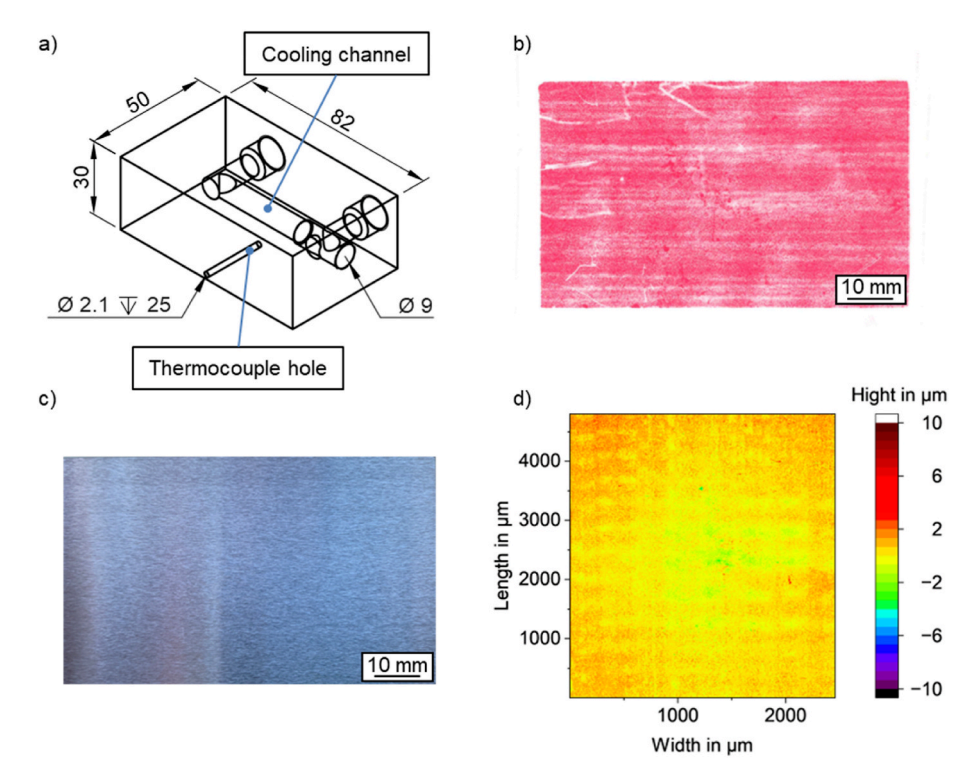


Fig. 6. a) isometric view of the stamp geometry, b) pressure distribution on the contact surface between the punches, c) real stamp surface and d) microscopic image of the surface roughness of a 4.5 × 2.5 mm section.

graphite-based heat-conducting paste is applied to ensure optimal heat transfer within the drilling and thus precise temperature measurement. The measurement and data acquisition of the sample and punch temperatures is carried out with the NI 9213 measuring amplifier from National Instruments at a frequency of 50 Hz. For reproducibility of the temperature measurement, the type N thermocouples of the sample are referenced before and after each test series using a calibrated type N thermocouple and the temperature deviation is taken into account as an offset. To ensure consistent process conditions, the heating unit is controlled and the acquisition of data is facilitated by utilizing the LabView graphical programming environment from National Instruments. The duration of the process, the punch and sample temperatures, the control voltage, and the pressure are systematically recorded.

The tool-based heat treatment is comprised of three phases: heating, solution heat treatment, and quenching (see Fig. 7 a)). The procedure is initiated with the clamping of the specimen in the test stand, followed by the positioning of the thermocouple within the frontally drilled hole. Subsequently, the heating unit is positioned between the punches. A tensile load of 100 N is applied to the sample by the thermal

compensation unit to prevent buckling due to thermal expansion. The sample is then heated at a linear heating rate of maximum 60 K/s. The heating phase ends as soon as a temperature of 10 K below the solution heat treatment temperature is reached. To prevent creep effects, the thermal compensation is switched off during this phase. During the solution heat treatment phase, the sample temperature is controlled by a PI controller to within ± 4 K, which corresponds to a deviation of 0.44 % from the set temperature (see Fig. 7 b)). The solution heat treatment is timed, and the pneumatic drive unit is manually actuated to start the specimen quenching process. Due to the high heat transfer coefficient and the low surface roughness, cooling rates of up to 1600 K/s are achieved within a temperature range of 800 °C–500 °C.

The recently developed test method for tool-based short-time heat treatment offers a potential for material-saving and process-oriented characterization of the TISTRAQ process on a laboratory scale. Resistance heating facilitates efficient, rapid, linear heating of the specimen with high heating rates and good control accuracy during the solution heat treatment process. Compared to heating in an electric furnace, resistive heating has a particularly high efficiency of 90–96 % due to the

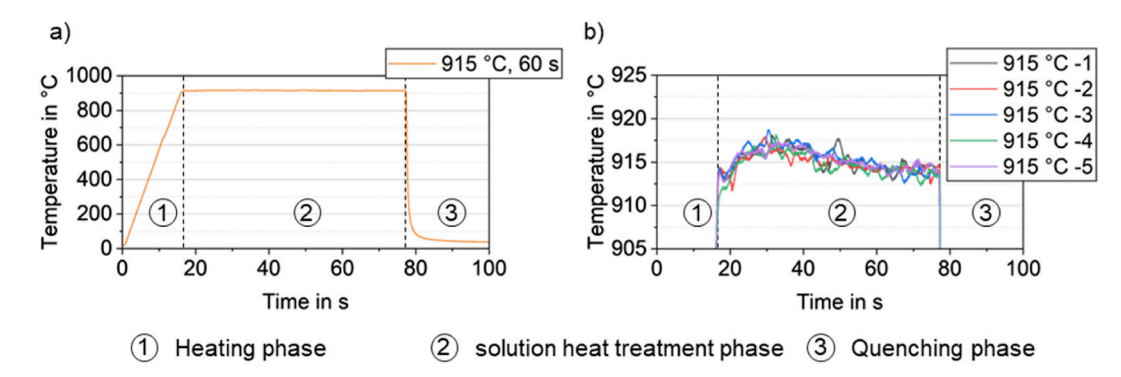


Fig. 7. Temperature profiles in the tool-based heat treatment test stand with the three phase 1. heating, 2. solution heat treatment, and 3. quenching: a) characteristic process sequence and b) control accuracy of the temperature at solution heat treatment temperature.

direct generation of heat in the material. In addition, the thermal mass to be heated is limited to the sample itself. This allows short process times due to the elimination of pre-heating time and high heating rates, resulting in particularly low energy consumption i.e. energy efficiency. The quenching unit, equipped with synchronous kinematics, facilitates the precise reproduction of cooling processes through direct tool contact, enabling cooling rates of up to 1600 K/s. The test stand is designed for autonomous operation, allowing for the configuration of flexible temperature profiles and the examination of diverse material combinations. Ensuring reproducibility is a primary concern and several measures have been implemented to this effect.

3.2. Temperature distribution as predicted from the simulation model

Fig. 8 shows the temperature distribution of the simulation model in the sheet metal strip from different viewing perspectives: a) top view (with position of the drilled hole of the thermocouple marked by an arrow), b) cross sectional views A-A and B-B (which are relevant regarding sampling for material characterization). From the top view perspective in Fig. 8 a), an influence of the drill hole on the simulated temperature distribution is clearly apparent. It was observed that the presence of the drill hole causes an asymmetric temperature distribution across the width of the specimen, spreading in an elongated oval shape and increasing the heated area towards the end of the drill hole. The maximum temperature of 918.7 °C is located at the center of the specimen, which is defined as the point positioned at the height of the drill hole, 5.5 mm in the width direction and 1 mm in the length direction. The localization of the maximum temperature at the specimen center and the elongated oval-shaped temperature distribution are attributed to the reduced cross-section at the drill hole location, which in turn leads to overheating at this point.

The underlying physical explanation for the occurrence of local overheating at the site of reduced area can be explained as follows: It is well established that in Joule heating, the electrical resistance is inversely related to the cross-sectional area. Consequently, a reduction in cross-sectional area, for example due to a drilled hole, results in a local increase in resistance. According to Joule's Law, this results in an increase in the locally generated heat output, which in turn causes

overheating in this area. This relationship has also been discussed in several studies, see for example [41-44].

As is apparent from the sectional views A-A and B-B in Fig. 8 b), the specimen exhibits also an inhomogeneous simulated temperature distribution across the width and the thickness of the sample. Due to the convection boundary conditions, the surfaces of the specimen exhibit lower temperatures compared to the interior of the specimen, and a gradual temperature gradient from the surfaces towards the center of the specimen. The temperatures appearing at a particular position in the A-A section are higher than those at the same position in the B-B section. It is further notable that in the B-B section, the temperature field appears to be slightly shifted from the center (in terms of width and thickness) along the width axis toward the 0-width-position, i.e. towards the nondrilled side of the sheet metal strip. In the experiment, the drill hole is filled with a thermocouple, which had to be accounted for the boundary conditions. However, as mentioned in the experimental section, the thermocouple was not included in the FE model. Hence, in a simplified approach the inner surfaces of the drill hole were excluded from the convection boundary condition. Otherwise, a heat sink would form in the drill hole, resulting in a more inhomogeneous temperature profile, likely diverging to a higher extent from the real temperature field than the results shown in Fig. 8.

The evaluation of the temperature at the node just at the root of the drilled hole in A-A proved that the target temperature of 915 $^{\circ}$ C at this position was successfully reached. A validation of the simulation by means of experimental values will follow in Section 3.5.

3.3. Material potential – microstructural evolution and mechanical properties

Fig. 9 displays SEM-BSE images of the following Ti-6Al-4V material states: AR, and RHTQ material states, more specifically the RHTQ-STQ standard and the RHTQ-STA standard (for designations compare Section 2.3.1).

The microstructure of the AR material is characteristic of a rolled and mill annealed material; it consists mainly of the α -phase (appears in gray/as shades of gray), while only a small amount of the β -phase (brighter phase) is present, being located along the α/α grain

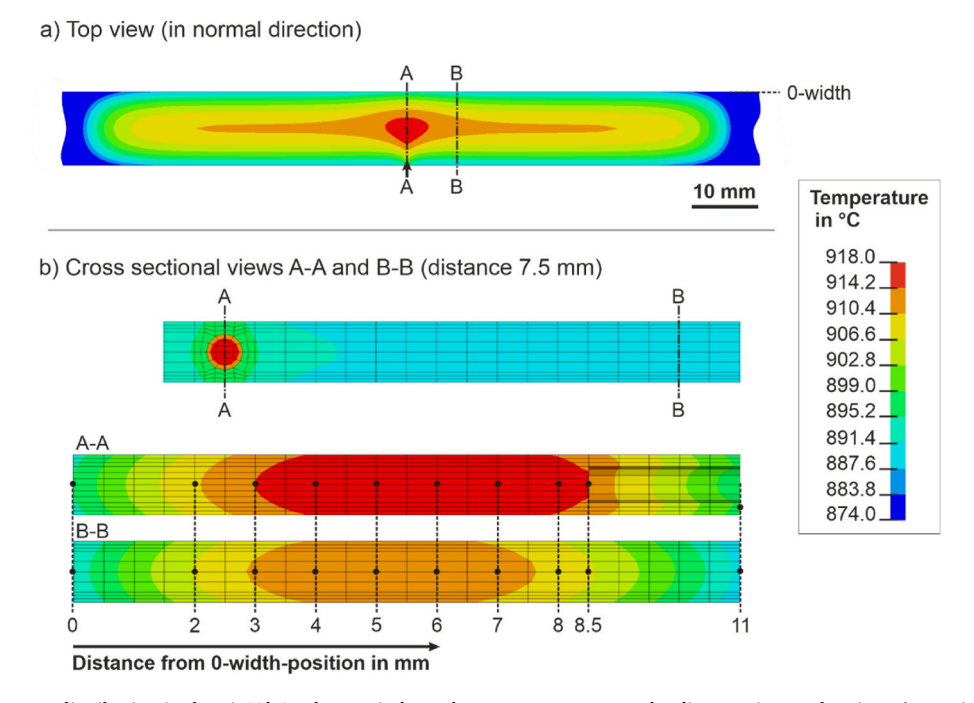


Fig. 8. Simulated temperature distribution in the Ti-6Al-4V sheet strip heated to target temperature by direct resistance heating: a) top view and b) cross sectional views. The FEM-simulation was performed with the *LS-DYNA* software, as described in Section 2.2.

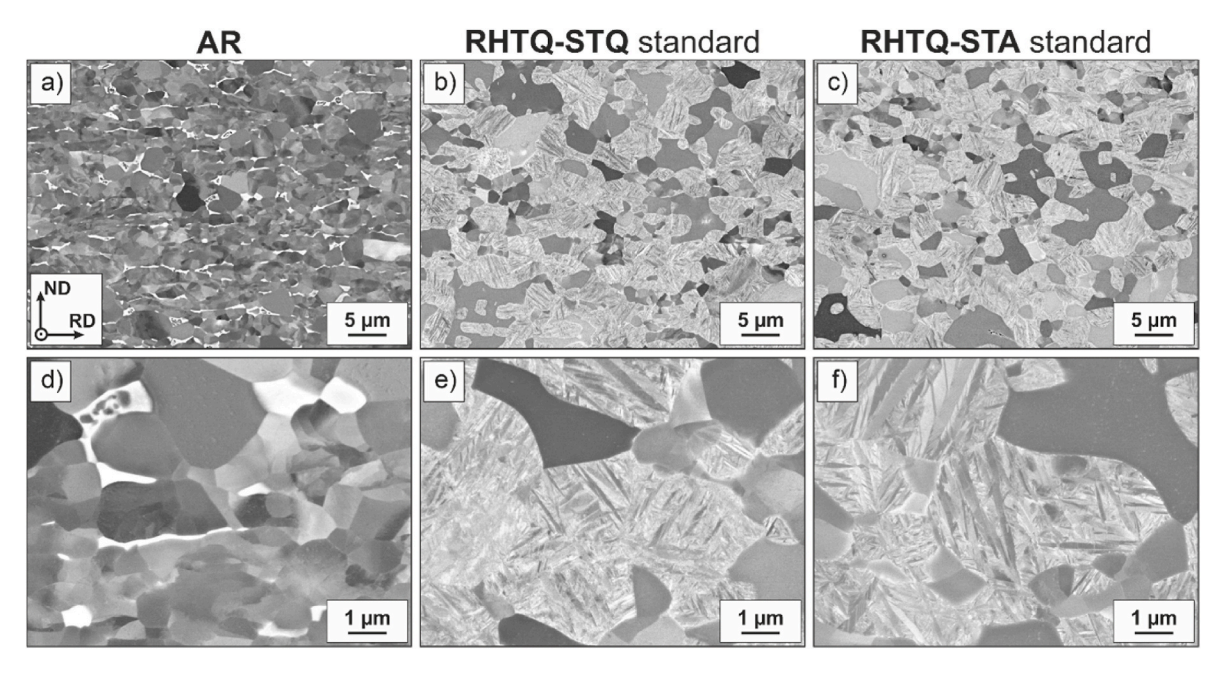


Fig. 9. SEM-BSE microstructural images of different Ti-6Al-4V material states: a) and d) AR-state, b) and e) short-time standard RHTQ-STQ state (60 K/s, 915 °C, 60 s, 10 MPa; for more details see Table 1) and c) and f) additionally short-time annealed RHTQ-STA state (RHTQ-STQ + 570 °C, 180 s, AC).

boundaries, compare Fig. 9 a) and d). A more detailed description of the starting material can be found in Ref. [23], where the same as-received material was used.

The RHTQ-STQ treatment results in a microstructure consisting of primary α -phase (α_p) and martensitically transformed β -phase (β_{trans}), compare Fig. 9 b) and e). This microstructure is due to the following aspects: solution heat treatment in the higher two-phase region results in an increased fraction of β -phase compared to AR, while subsequent toolbased quenching provides sufficiently high cooling rates to ensure a nondiffusional transformation of the prior β-phase to metastable hexagonal α' -martensite with the latter appearing as multiple plates in each prior β-grain. The dual phase nature, i.e. α -phase present next to α -martensite was proved by HEXRD measurements in Fig. A 1: in particular, the α/α' reflections are significantly broader compared to the AR-state due to the superposition of the spectra of hcp α -phase and the additional α' -phase. This broadening arises from slightly different lattice geometries between the two phases and the higher internal microscopic strain present in the α' -phase. The microstructural evolution is thus in general comparable to that shown in Ref. [23] for a short-time solution heat treatment in a vertical furnace followed by water quenching.

Although the mechanical data will be discussed in detail later, at this point we would like to highlight some of the potential characteristics of RHTQ-STQ conditions. Depending on the parameters, RHTQ-STQ conditions can either exhibit a lower yield strength and higher uniform elongation and work hardening than the AR material, as observed for example with a T_{ST} of 875 °C, compare Fig. 13. On the other hand, some RHTQ-STQ conditions may exhibit higher strength compared to the AR condition, with increased work hardening but at a slight decline of ductility, as observed for example with a T_{ST} of 915 $^{\circ}\text{C},$ compare Fig. 13. From a more general point of view, the mechanical properties in this material state are decisively influenced by the properties and the interaction of both microstructural constituents, the α -martensite and the alternating α_p -phase. The differing properties of these microstructural constituents result in a composite-like behavior under mechanical loading. In this context, the particular deformation behavior of α' -martensite, including the reorientation of specific α' -plates within a β-transformed grain, as extensively described by O. Dumas et al. [27,34] as the reorientation induced plasticity (RIP) effect, is assumed to play a crucial role.

In summary, the $\alpha+\alpha'$ microstructure that forms in the STQ-step is regarded to be beneficial for the targeted quench-parallel forming in the final TISTRAQ-process, provided that suitable process parameters are used. However, at this point it should be noted that the metastable state of the martensite constitutes a drawback for the direct technological application of the $\alpha+\alpha'$ -microstructures, especially when elevated application temperatures are considered. Furthermore, due to the martensitic transformation a volumetric change takes place which has the potential to strongly increase internal stresses.

From previous work, it was known that an additional short-time annealing can be carried out on STO Ti-6Al-4V material in order to strengthen of the material [23]. In this study, we also found that there is generally an increase in strength from each RHTO-STO state to its respective RHTQ-STA state. From a microstructural point of view, the RHTQ-STQ- and the corresponding RHTQ-STA states are indistinguishable from SEM-BSE alone, compare Fig. 9 b) and e) to c) and f). In Pfeffer et al. [23], results from nanohardness measurements in combination with HEXRD results have indicated that microstructural changes on the nanoscale occur within β_{trans} during the short-time annealing. More specifically, their HEXRD analysis revealed an initial stage of martensite decomposition into equilibrium $\alpha+\beta$ phases, since small β -peaks occurred in the STA-state, while the width of α/α' -peaks decreased. Further, they observed a significant increase of $\beta_{\text{trans}}\text{-hardness}$ from the STQ- to the corresponding STA-state. Thus, it is assumed that following an annealing at 570 $^{\circ}$ C for 180 s, fine β -precipitates form, contributing to the enhanced strength observed in $\beta_{\text{trans.}}$ However, further high-resolution techniques are required for a detailed characterization. In this work, it could be proved by HEXRD (appendix Fig. A 1) that the microstructure from RHTQ-STQ to RHTQ-STA follows the same trend previously observed from STQ-states produced in the vertical furnace followed by water quenching to the corresponding STA-state [23]. Specifically, there is a narrowing of α/α' -peaks and an emergence of small β-peaks.

It is also worth noting that Dumas et al. [34] reported recently, that the RIP-effect is suppressed after an annealing at 500 $^{\circ}$ C in the time range of 15 min to 6 h what was attributed to the decomposition of martensite. It is reasonable that such suppression may also occur after shorter annealing times.

From a technological point of view, according to our current

knowledge, a comparable microstructural evolution and strength increase from RHTQ-STQ to RHTQ-STA can also be achieved with an industrial furnace instead of a laboratory vertical furnace (as used in this work) by adjusting the annealing parameters. Furthermore, the specific selection of annealing parameters in the short-time regime seems to offer the possibility of specifically influencing strength and ductility, depending on the desired properties of the final component. However, a discussion of the last two aspects would go beyond the scope of this paper.

Fig. 10 illustrates the effect of RHTQ treatment on the near-surface region of the Ti-6Al-4V sheet material as well as on its surface condition by a comparison of AR-state and the RHTQ-STQ standard.

For the AR condition, the following applies: The microstructure in the near-surface region closely resembles that of the sheet interior, compare Fig. 10 a) to Fig. 9 a). Additionally, the surface is free of oxides, see Fig. 10 c). Thus, the AR sample is characterized by a typical graymetallic sheen, compare Fig. 10 e) and f).

For the RHTQ-STQ state, the SEM-BSE image in Fig. 10 b) reveals an oxygen-influence, which is manifested by an increased α -fraction in the near-surface region and gradates downwards up to $\sim\!15\text{--}20~\mu\mathrm{m}$ towards the interior of the sheet until the fractions are equal to the sample interior. This increased α -fraction close to the surface can be attributed to an increased content of oxygen as a result of its absorption by the material during RHTQ processing in ambient atmosphere; deliberately, the α -phase is stabilized by oxygen. Further, the surface of the RHTQ-STQ state is characterized by an oxide of $\sim 2\text{--}3~\mu\mathrm{m}$ thickness, see Fig. 10 d), and this oxide appears in brown on the sample surface, compare Fig. 10 e) and f). HEXRD identified the oxide as TiO2 Rutile type (compare Fig. A 1, Fig. A 2, and Fig. A 4).

Oxygen analysis with CGHE showed an increase of oxygen content related to a cuboid of $\sim\!3.8\times3.8\times1$ mm (comparable surface to volume ratio) from AR with 0.145 ± 0.007 wt.-% (eq. 1450 ± 70 ppm) to RHTQ-STQ with 0.273 ± 0.006 wt.-% (eq. 2730 ± 60 ppm). It should be specifically noted that the oxygen content given for each material state reflects an average of the oxygen content of the sample. It can be assumed that the oxygen content within the RHTQ-STQ sample, as in the AR, is still $\sim\!0.145$ wt.-% (eq. 1450 ppm), while it is significantly higher in the near-surface area and especially in the oxide. By CGHE after

polishing off the oxide it was possible to better distinguish between the oxygen content attributed to the oxide layer from that of the oxygenaffected subsurface region. The results from Fig. 10 f) indicate that the increased average oxygen content in the entire cuboid from AR to RHTQ-STQ can be attributed as follows: the oxygen content in the nearsurface region contributes to an increase of \sim 0.02 wt.-% (eq. 200 ppm), while the oxygen content in the oxide accounts for an additional ~ 0.1 wt.-% (eq. 1000 ppm). Since aerospace specifications, as for example AMS 4911, prohibit the presence of any oxide, α-case or an oxygen content in the alloy exceeding 0.2 wt.-% (eq. 2000 ppm), it is therefore necessary to implement a post-process surface treatment when considering the use of RHTQ parts for the aerospace industry. Potential methods include sandblasting, chemical milling, or vibratory grinding. In particular, with regard to the mechanical properties under cyclic mechanical loading, which can be strongly influenced by the surface finish, an evaluation of the effect of the surface treatment methods is required. Corresponding investigations on the influence of the surface condition of the RHTQ-STA material (untreated vs. post-process surface treated) on the fatigue properties are currently in progress.

3.4. Influence of critical process parameters on material properties

It is known from Section 3.2 that the temperature field in the resistance heated sheet metal strip is subject to a certain inhomogeneity. To ensure a reliable and systematic evaluation of the influence of process parameters, it was imperative to employ a consistent methodology. This involves the utilization of a uniform location for the microstructural examinations and extracting tensile test specimens from a designated area, as presented in Section 2.3.2, to ensure consistency in the data collection process.

Fig. 11 clarifies the effects of parameter variation of (i) solution heat treatment temperature and (ii) time delay before quenching on the T-t curves. While it is quite clear how the T_{ST} affects the T-t curve of the RHTQ-STQ step, the impact of t_{QD} is less straightforward. As well visible in Fig. 11 b), during the delay time the samples cool down at a slower cooling rate which was determined to $\sim\!30.4$ K/s. This remains the case until the water-cooled tools are closed to initiate quenching. Different t_{OD} result in different starting temperatures from which the samples are

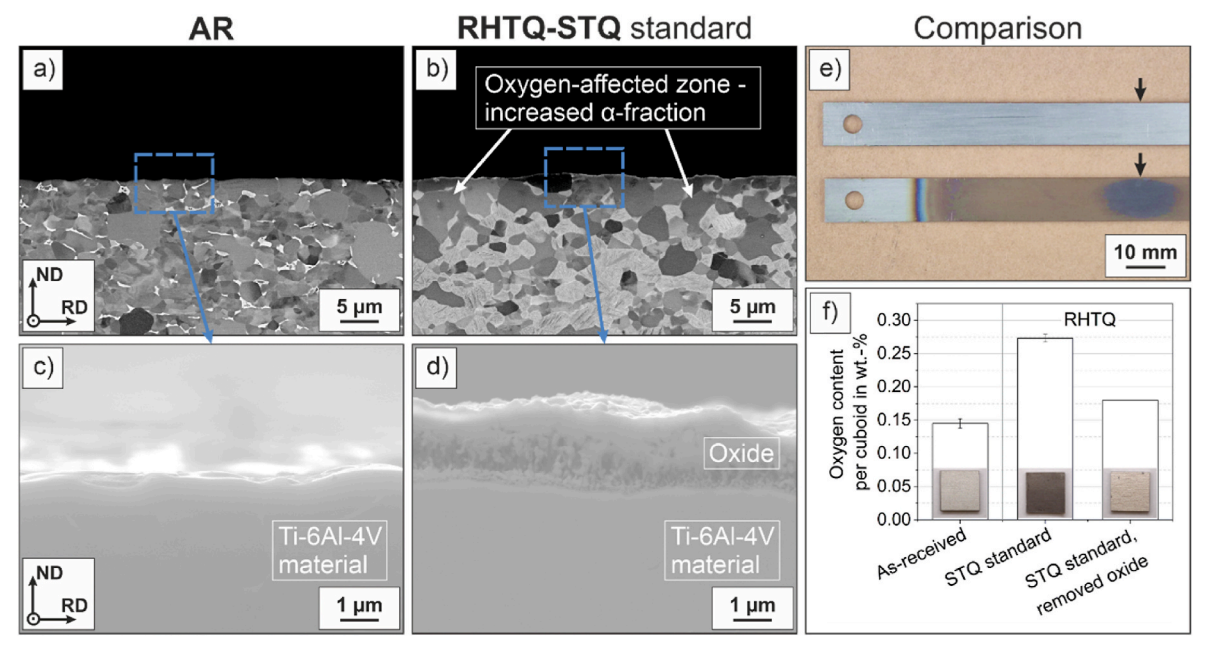


Fig. 10. SEM-BSE images of the near-surface region for a) AR and b) RHTQ-STQ standard reflecting the microstructure of the Ti-6Al-4V sheet material, SEM - SE images of the surface region for c) AR and d) RHTQ-STQ standard emphasizing the oxidation during RHTQ treatment, e) a comparison of AR and RHTQ-STQ sheet metal strips, and f) results of CGHE oxygen analysis.

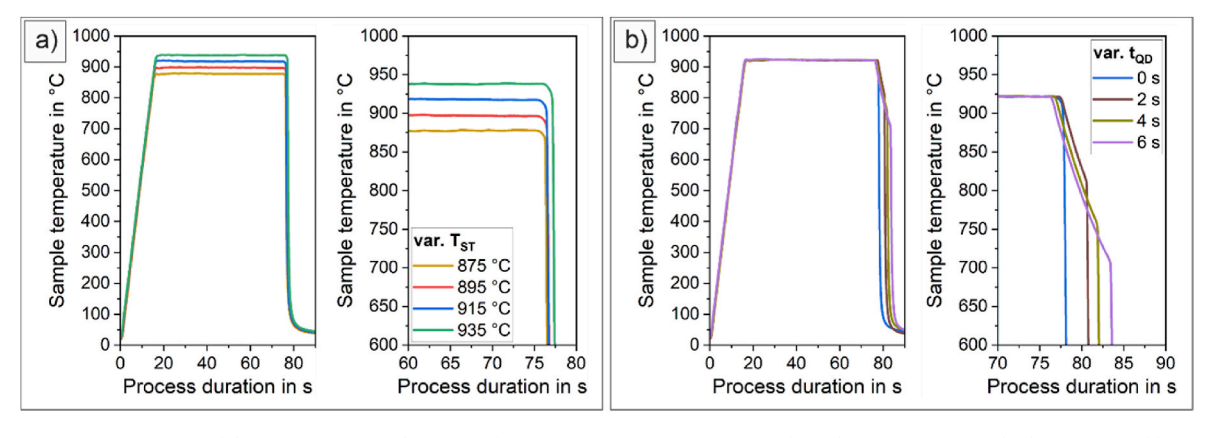


Fig. 11. Temperature-time curves of the RHTQ-STQ samples arising from parameter variations starting from the RHTQ-STQ standard (compare Table 1): a) variation of the solution heat treatment temperature T_{ST} (between 875 °C and 935 °C) and b) variation of the delay time to quenching t_{QD} (between 0 s and 6 s). The sample temperature was measured by a thermocouple placed in the drilled hole.

quenched with significantly higher cooling rates; the starting temperatures are ${\sim}810~^{\circ}\text{C}$ for $t_{QD}=2$ s, ${\sim}755~^{\circ}\text{C}$ for $t_{QD}=4$ s and ${\sim}700~^{\circ}\text{C}$ for $t_{QD}=6$ s.

3.4.1. Solution heat treatment temperature

SEM-BSE images of RHTQ-STQ samples for the lowest (875 $^{\circ}$ C) and highest (935 $^{\circ}$ C) nominal T_{ST} examined in this study are presented in Fig. 12. Relevant excerpts of the HEXRD spectra are provided in the Appendix (Fig. A 2).

These images in Fig. 12 demonstrate the trend of microstructural evolution as a function of the solution heat treatment temperature in the considered temperature range. With increasing T_{ST} from 875 °C to 935 °C, a significant change of the fractions of microstructural constituents can be observed; more precisely, the fraction of martensitically transformed prior β -phase increases, while the fraction of α_p decreases. This trend was to be expected on the basis of the thermodynamic data of the alloy system, which predict an increasing β phase fraction with increasing temperature, and is consistent with the trends reported in the literature [23–26]. The examination of HEXRD spectra of RHTQ-STQ

states as a function of T_{ST} reveals the presence of a dual phase $\alpha+\alpha'$ -microstructure as reported by Pfeffer et al. [23], compare Appendix Fig. A 2 c), e) and g). Further, slight differences in the shape and asymmetry of the α/α' -peaks indicate a change in the fractions and lattice parameters of the α' -martensite phase as function of T_{ST} . Additionally, the HEXRD results demonstrate that the oxide thickness increases with rising T_{ST} , which is expected due to the exposure of the material to higher temperatures (Fig. A 2 a); please note: the (110) TiO₂ Rutile peak is the highest among all Rutile peaks and is isolated, making it the most suitable for highlighting differences in the oxide.

A decrease in peak width of α/α' -peaks and the appearance of small β -peaks were observed in HEXRD spectra of RHTQ-STA states (see Fig. 2A d), f)) when compared to the RHTQ-STQ states. This observation provides evidence on an initial stage of decomposition of α' -martensite towards α_{eq} and β_{eq} on annealing temperature as a result of the short-time annealing. It thus aligns well with the proposed microstructural evolution by Ref. [23], and the latter seems to be applicable to the entire T_{ST} -range tested.

Fig. 13 shows representative stress-strain curves for the RHTQ-STQ

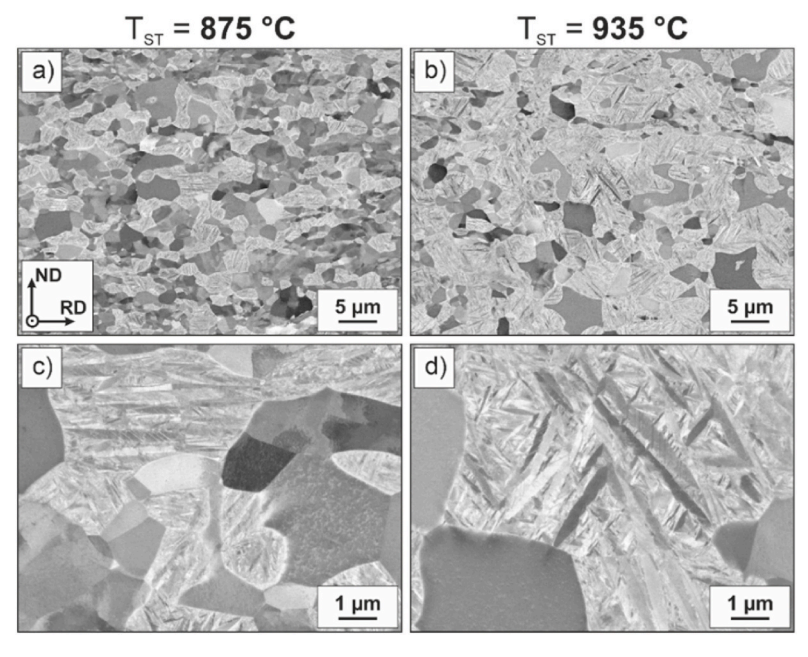


Fig. 12. SEM-BSE microstructural images of RHTQ-STQ material as function of the solution heat treatment temperature (60 K/s, var. T_{ST} , 60 s, 10 MPa): a) and c) $T_{ST} = 875$ °C and b) and d) $T_{ST} = 935$ °C. Images a) and b) are overview images that reflect the increase of β_{trans} fraction with increasing T_{ST} whereas close-up images of β_{trans}-grains c) and d) show the changing nature of the transformed microstructure as a function of T_{ST} ; the width of the α'-plates increases with increasing T_{ST} .

and the additionally short-time annealed RHTQ-STA conditions as a function of the $T_{\rm ST}$, along with the corresponding evolution of the mean characteristic values, which are further summarized in Table 2.

With increasing T_{ST} , the mechanical properties within the RHTQ-STQ process develop as follows from $T_{ST}=875\,^{\circ}\text{C}$ to $T_{ST}=935\,^{\circ}\text{C}$: the YS is highly sensitive to T_{ST} and increases; the UTS also increases but is less sensitive to T_{ST} compared to YS; the UEL and the ELF decrease with a significant drop ${>}895\,^{\circ}\text{C}$. After additional short-time annealing, the strength increases significantly compared to the respective RHTQ-STQ state at the expense of ductility to moderate values. Within the RHTQ-STA states, the trend with increasing T_{ST} follows parallel course with that observed in the RHTQ-STQ states: YS and UTS increase markedly (except from 915 $^{\circ}\text{C}$ to 935 $^{\circ}\text{C}$ STA) whereas UEL and ELF decrease, but this decrease is rather continuous, i.e. without a sudden change from one T_{ST} to the other.

These trends identified in this study for the effect of T_{ST} under RHTQ closely mirror those reported in previous work by Pfeffer et al. [23] for short-time solution heat treatments in a vertical furnace, in which the examination was performed on the same as-received material. This consistency supports the hypothesis that the same microstructural features govern the mechanical properties, regardless of the process-type applied.

In the aforementioned work [23], it was also shown that, in addition to the α_p and β_{trans} fractions and the α' -martensite plate size, the chemical composition of β_{trans} , the fractions of various interface types (α_D/α_D , α_D/β_{trans} , $\beta_{trans}/\beta_{trans}$) and the total interface line density also change with the TST. Furthermore, short-time solution treatments with different T_{ST} were found to result in a strong variability of the mechanical properties of STQ-states. For example, an increase in the hardness of β_{trans} with increasing T_{ST} was observed, which was attributed inter alia to the increasing Al content in the same direction, since Al is known to have a solid solution hardening effect. The numerous microstructural factors that are dependent on TST, the variable relative hardness between the two microstructural constituents α_{p} and β_{trans} related to the changing chemical composition of β_{trans} , the composite-like characteristics of the $\alpha+\alpha'$ dual phase Ti-6Al-4V microstructures in general and the rather stronger or weaker appearance of certain deformation mechanisms, such as the RIP-effect, were considered to be responsible for this high sensitivity of the mechanical properties across STQ-states. Furthermore, it was proved that the hardening from STQ to STA state is attributable to a hardening of $\beta_{\text{trans}}\text{,}$ what was attributed to an initial stage of α' -decomposition. The hardening potential of β_{trans} by additional short-time annealing was found to decrease with increasing T_{ST}; consequently, the V-content in β_{trans} (decreasing with increasing $T_{\text{ST}})$ was derived as playing a crucial role in this regard.

In comparison to Ref. [23], the determined phase fractions of the

RHTQ-STQ samples for a specific T_{ST} are higher in this work. This difference can be partially attributed to the inhomogeneity in the temperature distribution during RHTQ. Specifically, a higher actual temperature is expected in the center of the sample in the transverse direction (TD) than at the point used for analysis. Additionally, within the direct resistance heating technique and the sample geometry employed in this study, deviations between the actual temperature, the target temperature, and the simulated temperature are possible. These variations and their potential causes are discussed in more detail after the simulation validation in Section 3.5. It is plausible that these variations in phase fractions may contribute to the differences in mechanical properties between the RHTQ-STQ states in this study and the STQ states reported in Ref. [23]. Furthermore, the presence of an oxygen-influenced near-surface layer and higher residual stresses in the RHTQ-STQ states could also explain their comparatively higher strength observed.

In summary, the $T_{\rm ST}$ was identified as a critical parameter for the TISTRAQ-process. Therefore, it is imperative that the lowest possible deviation from the target temperature and a homogenous temperature distribution within the sheet metal strip prior to quench-forming is achieved in order to ensure successful process implementation.

3.4.2. Time-delayed quenching

Fig. 14 shows SEM-BSE images of RHTQ-STQ samples produced with $2\,s$, $4\,s$, and $6\,s$ time delays prior to quenching by means of water-cooled tools. Corresponding excerpts of HEXRD spectra are attached in the Appendix (Fig. A 4).

The SEM-BSE images in Fig. 14 reveal that the material states achieved for all three quenching delay times (2 s, 4 s, and 6 s) exhibit a slight decrease in the fraction of β_{trans} after RHTQ-STQ processing when compared to the standard RHTQ-STQ state with $t_{QD}=0$ s, as depicted in Fig. 9 b) and e). Additionally, the α/β_{trans} interfaces for all three states produced with toD depicted in Fig. 14 manifest a reduced smoothness compared to the standard RHTQ-STQ state. These two observations suggest that during cooling at a lower cooling rate, i.e. before the sheet metal strip is finally tool quenched, the α -phase expands from the α_p phase in the direction of the prior $\beta\mbox{-grains}.$ According to the thermodynamic properties of the Ti-6Al-4V system, a decrease in the T_{ST} would be expected to increase the α -phase content. However, for all three $t_{\mbox{\scriptsize OD}}$ RHTQ-STQ material states, the fraction of β_{trans} is larger than the theoretical equilibrium phase fractions at the quenching temperature would suggest. This finding indicates that the kinetics are too slow to allow full phase equilibrium to be established at the temperature within the short time exhibiting the slower cooling rate prior to quenching.

Regarding β_{trans} of $t_{QD}=2$ s and $t_{QD}=4$ s material states, $\alpha'\text{-martensite}$ can be concluded as transformed microstructure as it the

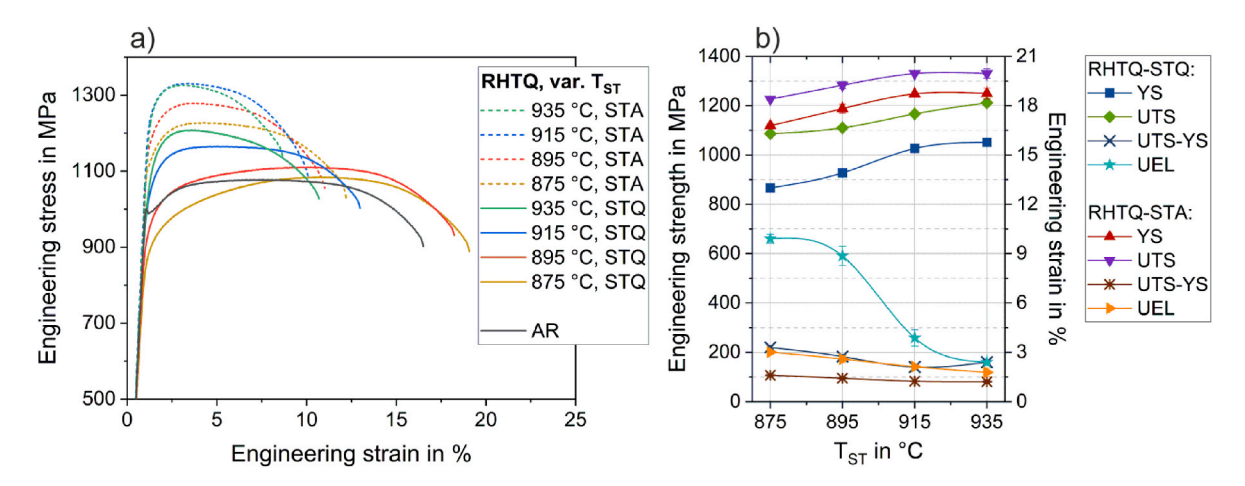


Fig. 13. a) Representative stress-strain curves of the RHTQ-STQ material states and RHTQ-STA material states (RHTQ-STQ + 570 °C, 180 s, AC) as function of the solution heat treatment temperature T_{ST} and b) overview of the corresponding evolution of mean characteristic values.

Table 2 Mechanical data as a function of solution heat treatment temperature T_{ST} for RHTQ-STQ material states and RHTQ-STA material states (RHTQ-STQ + 570 °C, 180 s, AC): yield strength at 0.2 % plastic deformation (YS), ultimate tensile strength (UTS), uniform elongation (UEL), and total elongation at fracture (ELF); based on at least three valuable tests (N \geq 3).

RHTQ-STQ, var. T_{ST}	YS in MPa	UTS in MPa	Δ UTS-YS in MPa	UEL in %	ELF in %	HV5
875 °C	866 ± 6.8	1086 ± 3.4	220 ± 7.1	9.9 ± 0.27	18.0 ± 0.31	347 ± 1.1
895 °C	927 ± 15.3	1110 ± 7.3	182 ± 8.5	8.9 ± 0.58	17.5 ± 1.66	347 ± 1.3
915 °C	1026 ± 4.2	1166 ± 1.0	140 ± 4.1	3.9 ± 0.50	11.9 ± 1.29	368 ± 2.3
935 °C	1051 ± 9.0	1211 ± 6.2	160 ± 4.8	$\textbf{2.4} \pm \textbf{0.11}$	$\textbf{8.7} \pm \textbf{1.61}$	380 ± 4.6
RHTQ-STA, var. T_{ST}	YS in MPa	UTS in MPa	Δ UTS-YS in MPa	UEL in %	ELF in %	HV5
RHTQ-STA, var. T _{ST}	YS in MPa 1119 ± 7.2	UTS in MPa 1226 ± 5.1	Δ UTS-YS in MPa 107 ± 6.2	UEL in %	ELF in %	HV5 384 ± 1.8
875 °C	1119 ± 7.2	1226 ± 5.1	107 ± 6.2	3.0 ± 0.12	11.5 ± 0.39	384 ± 1.8

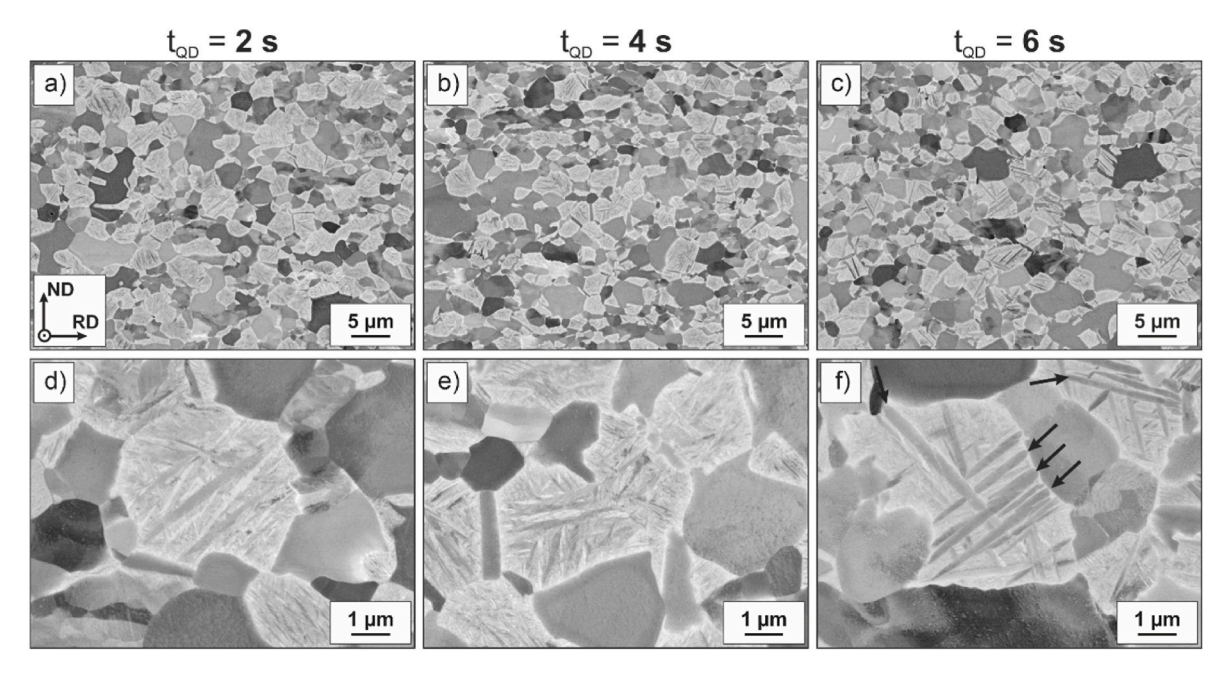


Fig. 14. SEM-BSE microstructural images of RHTQ-STQ material as function of the quenching delay time (60 K/s, 915 °C, 60 s, var. t_{QD} , 10 MPa): a) and d) $t_{QD} = 2$ s, b) and e) $t_{QD} = 4$ s c) and f) $t_{QD} = 2$ s. Images a)-c) are overview images, while d)-f) close-up images of β_{trans}-grains show the changing nature of the transformed microstructure as a function of t_{QD} ; at a t_{QD} of 6 s, α-lamellae marked by arrows indicate a partially diffusive transformation.

case for the standard RHTQ-STQ state with $t_{\rm OD} = 0$ s, and this is based on the observed characteristic plate-like structure in SEM-BSE images as well as taking into account the HEXRD data (Appendix: Fig. A 4). For $t_{\text{QD}}=6\ \text{s},$ however, lamellar structures can be observed in β_{trans} in the SEM-BSE images in Fig. 14 c) and f), which are distinct from the α' -plates. It can be posited that these are diffusely transformed α-lamellae. A magnified depiction of the transformed microstructure is provided in Appendix Fig. A 3. Consequently it is to be assumed that shortly before final quenching after $t_{QD}=6$ s, i.e. at 700 °C, a mixed microstructure of diffusionally formed secondary α -lamellae (α_s) and β-phase was present within the previous β-grains. Subsequent quenching then likely transformed the remaining β-phase. The HEXRD results provide further evidence to support this hypothesis. It is noteworthy to observe the peak at $2\theta = 4.24$ (TiO₂ Rutile peak position) in Fig. A 4 e), which exhibits equivalent height for $t_{OD} = 0-4$ s but is distinctly elevated for $t_{OD} = 6$ s. Additionally, it is evident that the highest TiO_2 Rutile peak in Fig. A 4 a) remains constant for all conditions, suggesting that the oxide thickness does not undergo changes with t_{QD} within the tested range. This observation indicates that the increased height of the peak at $2\theta = 4.24$ for $t_{QD} = 6$ s is attributable to the presence of additional metastable β -phase (β_m), which overlaps with the TiO₂ Rutile peak. Additionally, the shoulder of the (102) α/α' -peak in the $t_{QD}=6$ s

spectrum and the additional elevation between the two α/α' -peaks in Fig. A 4 c) indicate differences in the present phases compared to shorter top.

In summary, the findings suggest a RHTQ-STQ microstructure of type $\alpha+\alpha'$ for $t_{QD}=2$ s–4 s and a $\alpha+(\alpha_s+\alpha'+\beta_m)$ type structure for $t_{QD}=6$ s, with the brackets describing the transformed microstructure of the prior β -phase. At this point, it should be noted that the V-content in the β -phase just before quenching influences martensite formation: an increasing V-content reduces the driving force for martensite formation, lowers the martensite start temperature, and decreases the critical cooling rate [45,46]. The first two factors may explain the observed partially diffusional transformation structure in case of $t_{QD}=6$ s compared to the other RHTQ-STQ conditions.

For the RHTQ-STA $t_{QD}=2$ s–4 s conditions, additional β -peaks appear compared to the corresponding RHTQ-STQ conditions, see Fig. A 4 d) and f). In the RHTQ-STA $t_{QD}=6$ s spectrum, the β -peak heights increase and the peaks are shifted towards higher angles. This indicates a smaller lattice parameter of the newly formed β -phase than for β_m of the RHTQ-STQ condition, suggesting either a higher V-content [47] or a different composition in general, involving also other elements. Furthermore, within the RHTQ-STA states an increasing β phase fraction with increasing t_{QD} can be derived from increasing t_{QD} beak heights, what

can be likely be attributed to different chemical compositions of the prior as-quenched $\alpha^\prime\text{-martensite}.$

Fig. 15 shows stress-strain curves for the RHTQ-STQ and RHTQ-STA conditions as a function of $t_{\rm QD}$ and the corresponding evolution of mean characteristic values. The latter are additionally summarized in Table 3.

Within the RHTQ-STQ states, a time delay until quenching appears to have similar effects on the stress-strain curves as a reduction in the solution heat treatment temperature; with increasing time delay top, a decrease in YS and UTS is evident, and the strain values UEL and ELF exhibit an increase from $t_{QD}=0$ s to $t_{QD}=4$ s. The YS is much more sensitive to a variation in $t_{\mbox{\scriptsize QD}}$ compared to the UTS, a phenomenon that was also observed in the context of T_{ST} variations. These observations align quite well with the changes in microstructure observed with increasing quenching delay, which follow a similar trend to those found with decreasing T_{ST} . Specifically, an increasing fraction of the α -phase is observed with longer toD, while the fraction of martensitic transformed β-phase decreases. Due to the slower cooling rates during time delay and the resulting diffusion processes and element partitioning, it can also be expected that the V-content within the martensitically transformed β -phase increases with t_{QD} , while the Al-content decreases. This would also be comparable to the microstructural trend of a decreasing T_{ST}, as shown in the previous section of this work and in Ref. [23]. However, an additional decrease in UEL and ELF can be observed from RHTQ-STQ 4 s-6 s, besides the decrease in strength. This phenomenon may be attributable to the distinct transformation structure observed in this condition when compared to the other conditions for lower top. It is conceivable that the secondary alpha-lamellae within β_{trans} lead to earlier necking and failure due to their unfavorable geometry. The strength trend within the RHTQ-STA states as a function of toD roughly follows that of the RHTQ-STQ states; as toD increases, the achievable strength decreases and the strain values increase across all quenching delay times. However, it can be derived from Fig. 15 b), that t_{OD} has a linear effect on the strength values within the RHTQ-STA states, whereas it is non-linear within the RHTQ-STQ states. Furthermore, the work hardening potential remains relatively constant for RHTQ-STA as function of t_{OD}, while it exhibits an increase for RHTQ-STQ. Further, the relative losses demonstrate significant variation between RHTQ-STQ und -STA: the final values for $t_{QD} = 6$ s set in relation to the values for $t_{QD}=0\ s$ for YS-STQ, UTS-STQ, YS-STA, and UTS-STA are 81.7 %, 94.1 %, 86.3 %, and 90.2 %, respectively. Accordingly, it can be stated that the additional short-time annealing helps to even out larger differences resulting from t_{OD} effects of the RHTQ-STQ step.

Overall, it can be concluded that the t_{QD} also clearly represents a critical value for the TISTRAQ-process. Delayed quenching in the RHTQ-STQ step results in lower strengths in the final RHTQ-STA material state. In order to achieve the most homogeneous material properties, the time

between the end of the hold at the target temperature and the quenching of the Ti-6Al-4V sheet must be kept as short as possible within the whole sheet metal strip or blank, and this is also relevant for achieving most effective strengthening.

3.5. Validation of the simulation and linking of results

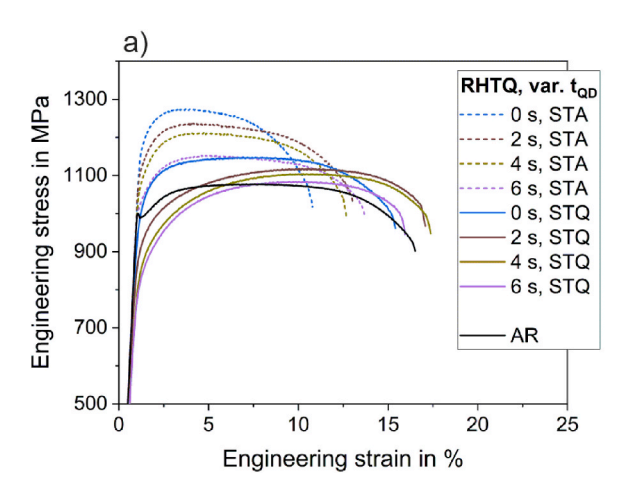
As shown in Section 3.4 and in the extant literature [23–26] there is a strong correlation between solution heat treatment temperatures and phase fractions of α_p and β on temperature and α_p and β_{trans} after quenching, respectively. Thus, the phase fractions in the RHTQ-STQ sheet metal strip can be used as an indirect measure of T_{ST} distribution. A determination of the phase fractions in turn facilitates a comparison with the trends from the temperature simulation and thus allows for a qualitative experimental validation of the simulation results.

Therefore, a selection of nodes was made from the cross sections A-A and B-B and the nodes' temperatures were extracted from the simulation results presented in Fig. 8 b). Furthermore, the phase fractions were evaluated for Ti-6Al-4V RHTQ-STQ sheet metal strips at the positions of the selected nodes. The estimation of the phase fractions was carried out by binarization of SEM-BSE-images of 100 μm width in Image J Fiji [48] and thereby making use of the Trainable Weka Segmentation plugin [49]. The determined β_{trans} fractions for RHTQ-STQ standard sheet metal strips across A-A and B-B are presented in Fig. 16, alongside the simulated T_{ST} .

The development of the fractions of β_{trans} along the cross-sections A-A (Fig. 16 a)) and B-B (Fig. 16 b)) indicates a qualitative consistency between the experimental and simulated results. The highest phase fractions and simulated temperatures are observed in the center of the sheet metal strip (at 5 mm and 6 mm), with a decrease towards the positions of 0 mm and 11 mm. The cross-section B-B exhibits lower maximum phase fractions compared to A-A, indicating lower temperatures in the sheet metal strip, a finding that aligns with the simulation results.

Furthermore, the results of the phase analysis demonstrate that the simulation slightly underestimates the temperature inhomogeneity, compare Fig. 16 a). Given the nearly linear correlation between temperature and phase fractions within this temperature range, the observed discrepancies in phase fractions from the edge to the center suggest potential discrepancies in temperature between the simulation and experimental results. These discrepancies could be attributed to potential inaccuracies in the assumed values for electrical and thermal conductivity in the simulation, which may not accurately reflect the actual values.

In comparison with Pfeffer et al. [23], the phase fractions at the bottom of the hole suggest that the actual temperature exceeded the



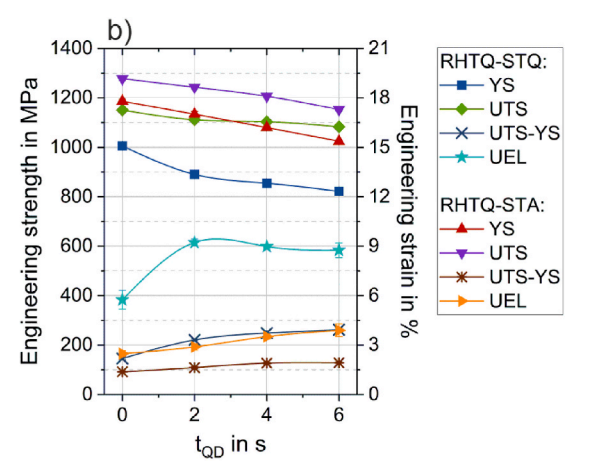


Fig. 15. a) Representative stress-strain curves of the RHTQ-STQ material states and the RHTQ-STA material states (RHTQ-STQ + 570 °C, 180 s, AC) as function of the quenching delay time t_{OD} and b) overview of the corresponding evolution of mean characteristic values.

Table 3 Mechanical data as a function of quenching delay time t_{QD} for RHTQ-STQ material states and RHTQ-STA material states (RHTQ-STQ + 570 °C, 180 s, AC): yield strength at 0.2 % plastic deformation (YS), ultimate tensile strength (UTS), uniform elongation (UEL), and total elongation at fracture (ELF); based on at least three valuable tests (N \geq 3).

RHTQ-STQ, var. $t_{\rm QD}$	YS in MPa	UTS in MPa	Δ UTS-YS in MPa	UEL in %	ELF in %	HV5
0 s	1006 ± 5.6	1151 ± 3.7	145 ± 4.1	5.7 ± 0.57	13.1 ± 2.20	353 ± 1.3
2 s	891 ± 8.6	1111 ± 7.1	221 ± 3.5	9.2 ± 0.21	17.1 ± 1.15	330 ± 2.1
4 s	855 ± 12.4	1102 ± 3.9	248 ± 9.4	9.0 ± 0.08	16.1 ± 0.18	333 ± 2.8
6 s	822 ± 4.73	1083 ± 3.49	261 ± 2.2	8.8 ± 0.45	15.2 ± 0.73	329 ± 1.2
RHTQ-STA, var. $t_{\rm QD}$	YS in MPa	UTS in MPa	Δ UTS-YS in MPa	UEL in %	ELF in %	HV5
RHTQ-STA, var. t _{QD}	YS in MPa 1186 ± 8.0	UTS in MPa 1278 ± 8.6	Δ UTS-YS in MPa 92 ± 3.0	UEL in %	ELF in %	HV5 388 ± 1.9

0 s	1186 ± 8.0	1278 ± 8.6	92 ± 3.0	2.5 ± 0.17	8.9 ± 1.72	388 ± 1.9

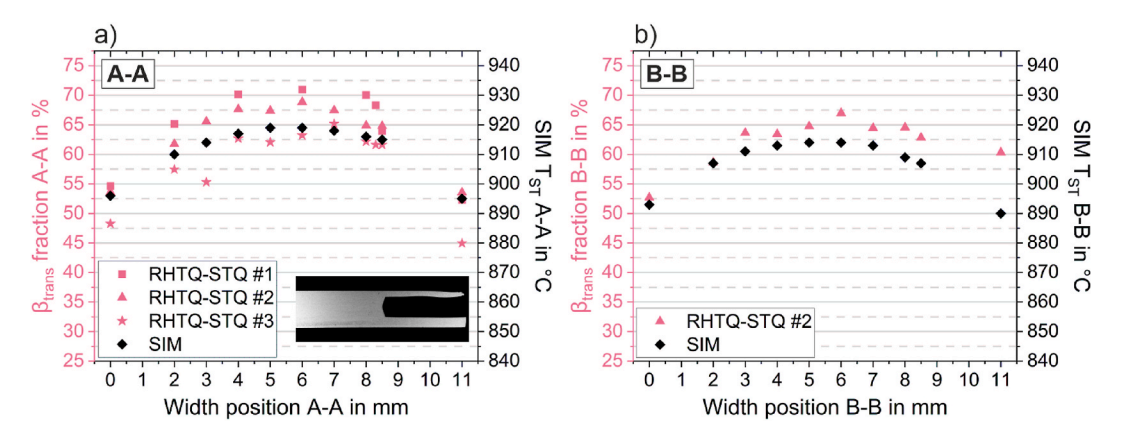


Fig. 16. Experimentally determined fractions of β_{trans} and simulated temperatures across the width of a) the A-A and b) the B-B cross-section (see Fig. 8 for details). Samples #1-#3 for microstructural analysis in a) were produced in different experimental series over time, reflecting series-related scatter due to material- and procedure-related factors.

target temperature. This discrepancy may be attributable to the temperature measurement technique used in this work. The mismatch between the cone-shaped geometry of the bottom of the hole and the different rounded shape of the thermocouple could cause the thermocouple to measure a temperature at another location that is lower than the actual temperature at the bottom of the hole. Furthermore, the graphite-based heat-conducting paste is not incorporated into the simulation, which can also result in deviations in the absolute temperatures. The discrepancy could also be attributed to the heat flow over the external area of the thermocouple, which is not heated but is situated in the ambient atmosphere. The scattering of the phase fractions in cross-section A-A across different RHTQ-STQ sheet strips, Fig. 16 a), also

indicates measurement influences.

In future studies, the aim is to adapt the TISTRAQ-process to an industrial scale and to validate it using a demonstrator of an adjusted S-Rail part geometry that is well established in the field of sheet metal forming. Therefore Fig. 17 provides an outlook on the further application of the simulation methodology. The insights gained from the simulation setup and the definition of boundary conditions for the Ti-6Al-4V sheet metal strip have been incorporated into the process chain modeling of the S-Rail component. A key difference between the resistive heating setup for the S-Rail blank and the sheet metal strip from Section 3.2 lies in their modeling approach. While the sheet metal strip is represented with solid elements, the S-Rail blank is modeled using shell

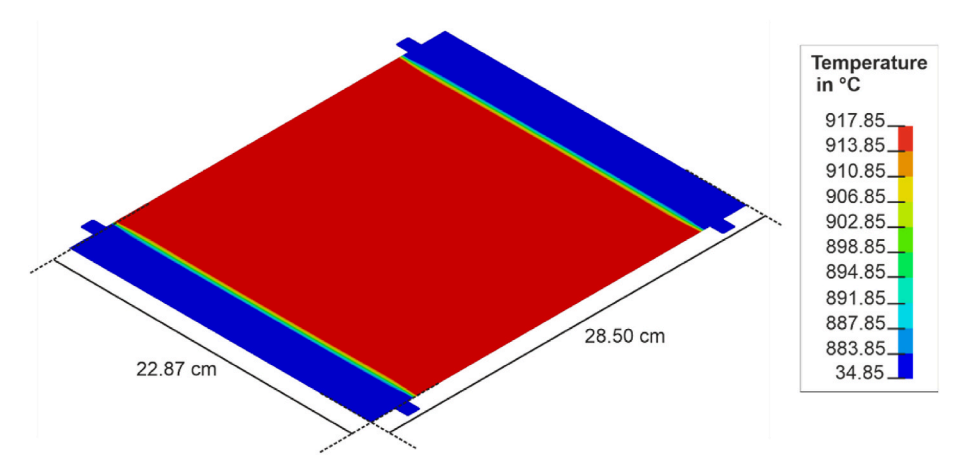


Fig. 17. Simulated temperature distribution of the resistance heated blank in the forming simulation of the S-Rail part.

elements, which is more efficient for large scaled forming parts. Additionally, unlike the sheet metal strip, the S-Rail blank does not feature a drill hole for temperature measurement; instead, temperature monitoring is conducted using a pyrometer. This ensures that the influence on the cross-section of the S-Rail blank is eliminated, thereby promoting temperature homogeneity. The boundary conditions are applied analogously to those used for the sheet metal strip.

4. Summary and conclusions

The following conclusions can be drawn:

- A novel test method was developed to characterize tool-based heat treatment on a laboratory scale. The corresponding test stand consists of a resistance heating unit for solution heat treatment and a tool-based quenching unit for quenching the specimen afterwards. This enables the implementation of heat treatment with flexible temperature profiles in the TISTRAQ-process, which is both energyefficient and material-saving.
- The advantages of the test stand are its autonomous operation, the good control behavior and the high reproducibility of defined temperature profiles with a linear heating rate. The direct heat generation in the sample enables temperatures of up to 1200 °C with heating rates up to 60 K/s. The synchronous kinematics and the wide force spectrum facilitate the realistic reproduction of process conditions during quench-forming, enabling cooling rates of up to 1600 K/s.
- The application of the FE-simulation model for resistance heating proved to be valuable even before the initial investigations, as it provided an early understanding of the temperature distribution within the sheet metal strip. Subsequent experimental studies then served as a qualitative validation of the simulation, confirming that it effectively captured the overall temperature distribution. However, the results also revealed that the simulation underestimates the temperature inhomogeneity, highlighting areas for further refinement.
- Direct electric resistance heating of a Ti-6Al-4V sheet metal strip to a nominal target solution heat treatment temperature in the range 875 $^{\circ}\text{C}$ –935 $^{\circ}\text{C}$ followed by quenching in water-cooled tools in the developed test stand results in $\alpha+\alpha'$ -microstructures. As a result of processing in ambient atmosphere, the near-surface region shows an oxygen-influenced surface-near layer and an oxide of thickness, which necessitates a post-processing surface treatment for specific applications. Subsequent short-time annealing results in a significant increase in strength compared to the $\alpha+\alpha'$ -state and the initial asreceived material state.
- The developed test stand facilitates a systematic investigation of the influence of various process parameters. The solution heat treatment temperature (varied in the range 875 °C–935 °C) and the time delay until quenching (varied in the range 0 s–6 s) were identified as critical values for the TISTRAQ-process. The microstructure and mechanical properties are highly sensitive to the variation of these two parameters, both in the resistively heated and tool-quenched state and after additional short-time annealing. For the successful implementation of the TISTRAQ-process for the production of Ti-6Al-4V sheet metal parts with homogeneous properties, it is

- therefore crucial to minimize variations in the temperature distribution and the time delay until quenching.
- The results of the current investigations form the basis for the
 development of a promising forming process suitable for series production for aviation-specific applications, thereby evoking strength
 enhancement. The new TISTRAQ-process addresses both the sustainability and lightweighting aspects of the aerospace industry and
 will be extended to larger scale and more complex part geometries in
 future investigations.

CRediT authorship contribution statement

N. Pfeffer: Conceptualization, Investigation, Methodology, Validation, Data curation, Visualization, Writing - original draft (Sections: 1 partially, 2.3 - fully, 3.3 - fully, 3.4 - fully, 3.5 - partially, and overarching merge), Writing - review and editing; M. A. Kaiser: Conceptualization, Investigation, Methodology, Validation, Data curation, Visualization, Writing - original draft (Sections: 1 - partially, 2.1 - fully, and 3.1 - fully), Writing - review and editing; W. Feix: Investigation, Methodology, Visualization, Data curation, Writing - original draft (2.2 - fully, 3.2 - fully, and 3.5 - partially); N. Kälble: Methodology, Investigation; M. Merten: Methodology; A. Stark: Methodology and investigation (HEXRD); A. Haufe: Supervision, Writing - review and editing, Resources, Conceptualization, Funding acquisition, Project administration; T. Meyer: Resources, Conceptualization, Funding acquisition, Project administration, Supervision; T. Tröster: Supervision, Writing review and editing; H. W. Höppel: Supervision, Writing - review and editing, Conceptualization, Resources, Funding acquisition, Project administration.

Institution contribution statement - specified main topics

^aFAU – Institute for General Materials Properties: Annealing, Microstructural and mechanical characterization and evaluation, ^bLiA and ^dHEGGEMANN AG: Test stand design and RHTQ-STQ sample production, ^cDYNAmore GmbH: Simulation, ^eHereon: HEXRD methodology and investigation.

Declaration of competing interest

The authors declare that they have no known competing financial interests or personal relationships that could have appeared to influence the work reported in this paper.

Acknowledgments

The authors acknowledge funding from the Federal Ministry for Economic Affairs and Climate Action under the LUFO-VI program for the joint research project TISTRAQ, with funding reference 20Q1927. Partners in this project are HEGGEMANN AG, the Institute I of FAU and the DYNAmore GmbH, an Ansys company. Further, the authors express their gratitude to the Deutsches Elektronen Synchrotron, DESY (Hamburg, Germany), a member of the Helmholtz Association HGF, for the provision of experimental facilities. Parts of this work were carried out at PETRA III/P07-High Energy Materials Science beamline. Beamtime was allocated for proposal I-20230881. We further sincerely thank Jan-Niklas Wesendahl for providing material data for the simulations.

Appendix

HEXRD-data: AR \longleftrightarrow RHTQ-STQ standard \longleftrightarrow RHTQ-STA standard

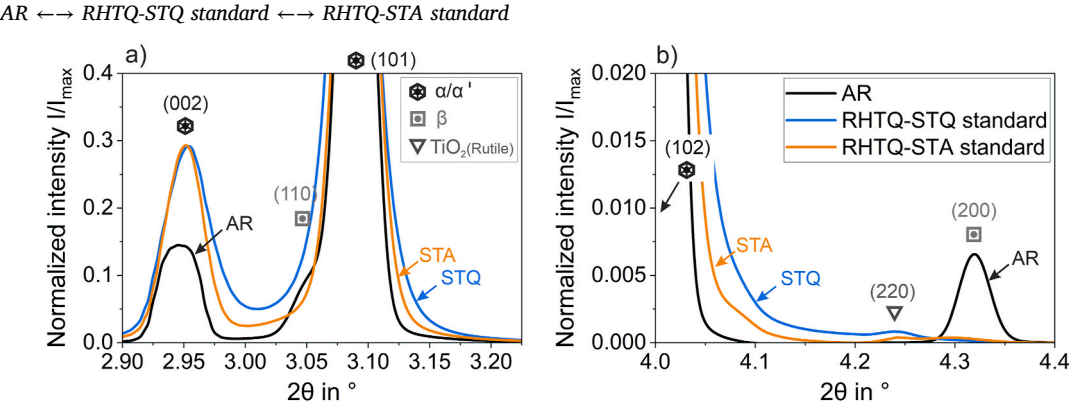


Fig. A 1. Selected representative excerpts from the HEXRD spectra of different material states: AR, RHTQ-STQ standard, and RHTQ-STA standard.

HEXRD-data: RHTQ with var. T_{ST}

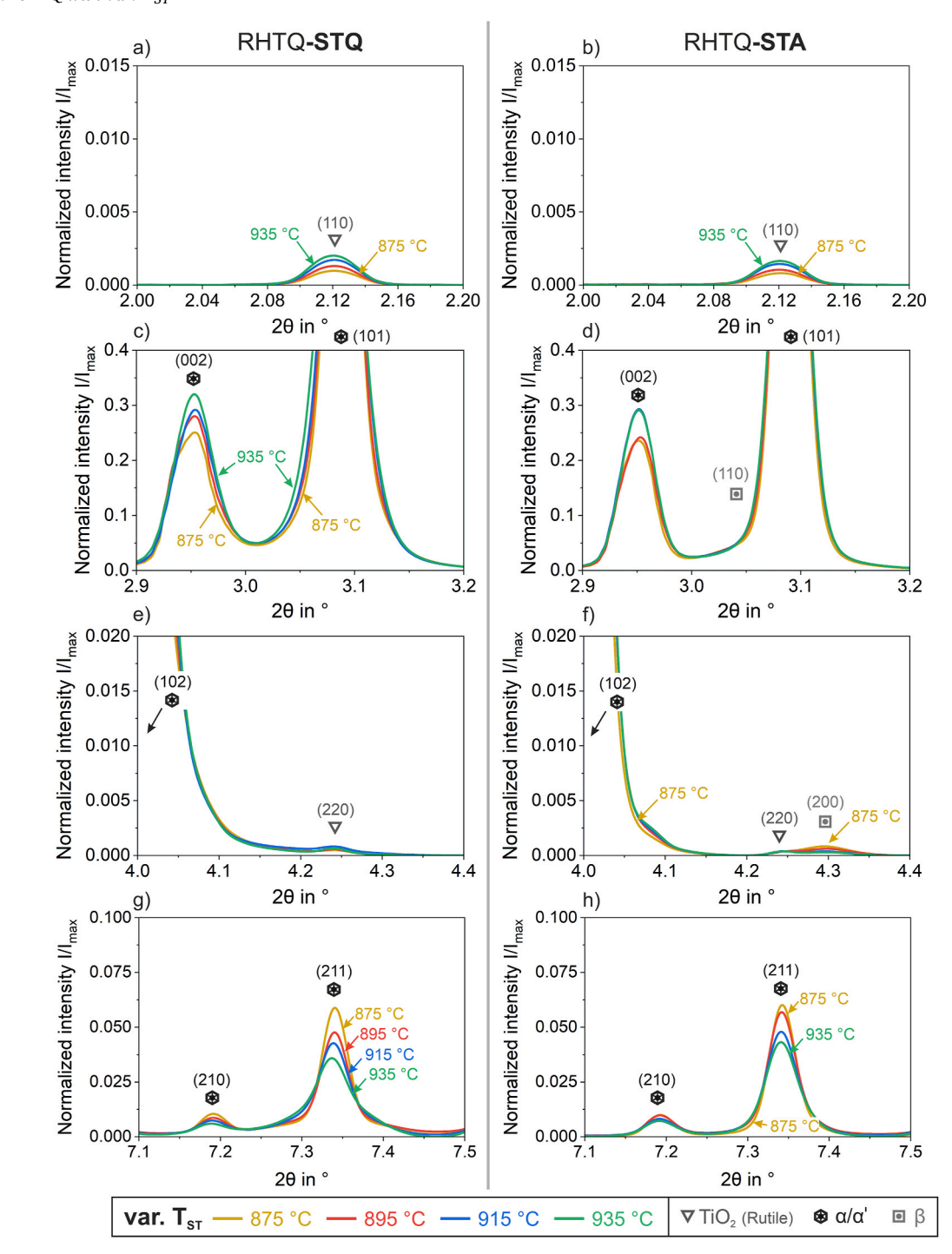


Fig. A 2. Selected representative excerpts from the HEXRD spectra of different material states: a), c), e), g) RHTQ-STQ states with varying solution heat treatment temperature T_{ST} (further parameters compare Table 1), and b), d), f), h) corresponding RHTQ-STA states (RHTQ-STQ + 570 °C, 180 s, AC).

SEM-BSE-image and HEXRD-data: Time-delayed quenching

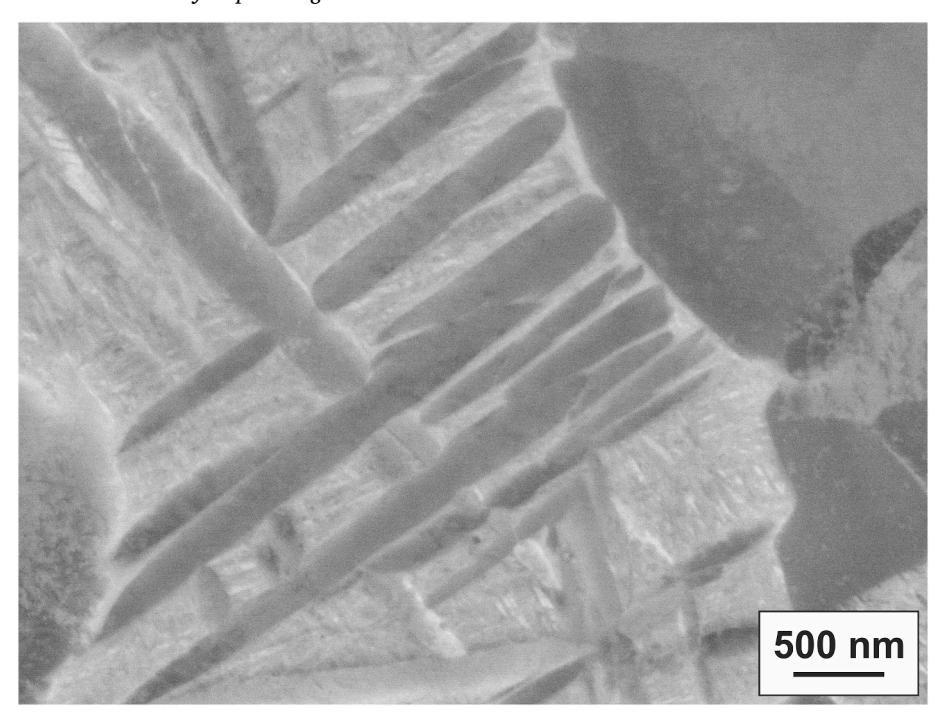


Fig. A 3. Enlarged depiction of the RHTQ-STQ samples produced with $t_{QD}=6\ s$, as shown in Fig. 14 f).

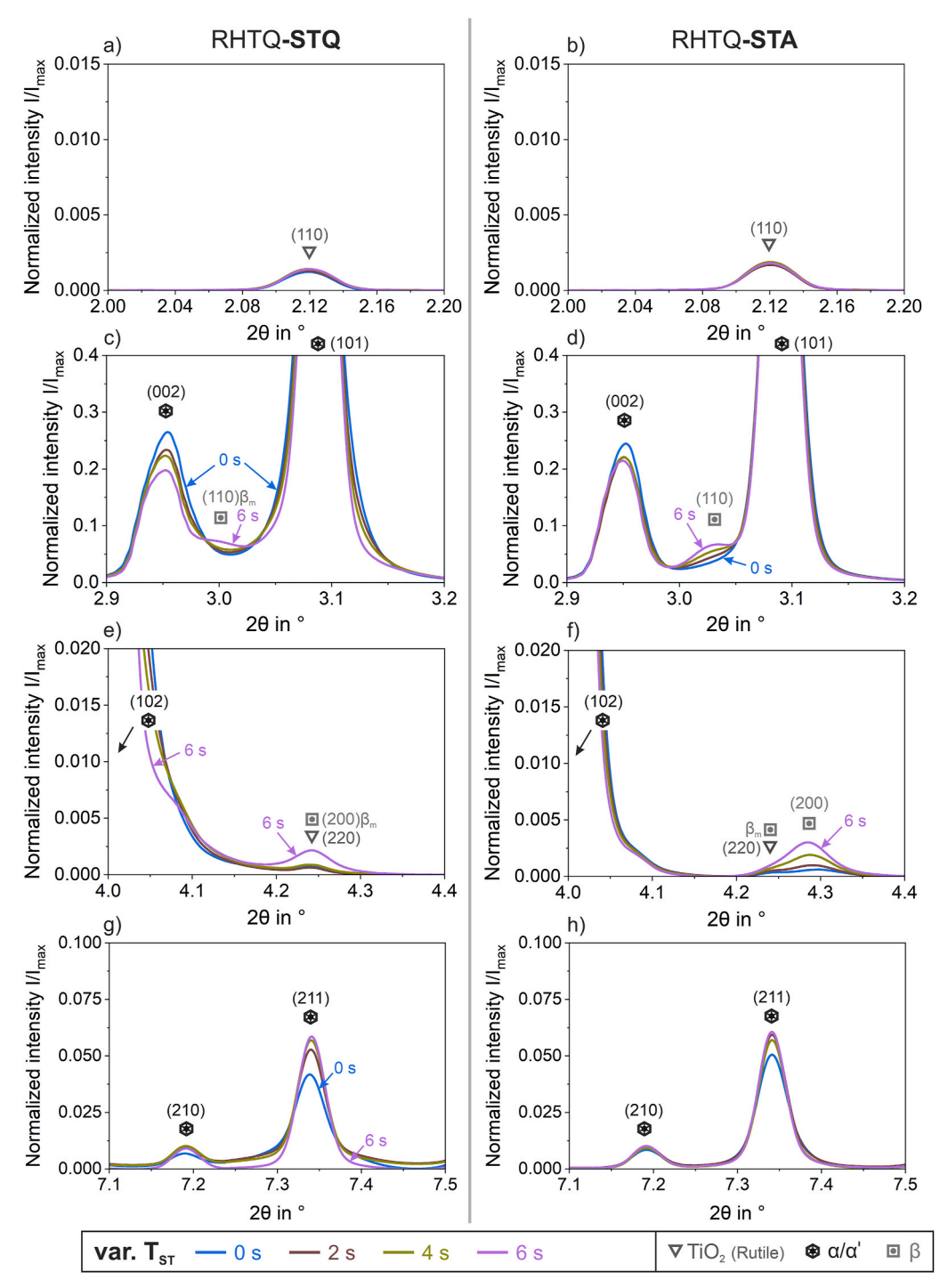


Fig. A 4. Selected representative excerpts from the HEXRD spectra of different material states: a), c), e), g) RHTQ-STQ states with varying quenching delay time t_{QD} (further parameters compare Table 1), and b), d), f), h) corresponding RHTQ-STA states (RHTQ-STQ + 570 °C, 180 s, AC).

Data availability

Data will be made available on request.

References

- J. Peirs, P. Verleysen, J. Degrieck, Study of the dynamic bauschinger effect in Ti6Al4V by torsion experiments, EPJ Web Conf. 26 (2012) 01023, https://doi.org/ 10.1051/epjconf/20122601023.
- [2] G. Lütjering, J.C. Williams, Titanium, second ed., Springer, Berlin, 2007.
- [3] O.M. Badr, B. Rolfe, P. Hodgson, M. Weiss, Forming of high strength titanium sheet at room temperature, Mater. Des. 66 (2015) 618–626, https://doi.org/10.1016/j. matdes.2014.03.008.
- [4] H. Hoffmann, R. Neugebauer, G. Spur, Handbuch Umformen, Hanser Verlag, München, 2012, https://doi.org/10.3139/9783446430044.
- [5] R. Neugebauer, T. Altan, M. Geiger, M. Kleiner, A. Sterzing, Sheet metal forming at elevated temperatures, CIRP Ann 55 (2006) 793–816, https://doi.org/10.1016/j. pips/000610006
- [6] F. Ozturk, R.E. Ece, N. Polat, A. Koksal, Z. Evis, A. Polat, Mechanical and microstructural evaluations of hot formed titanium sheets by electrical resistance heating process, Mater. Sci. Eng. A 578 (2013) 207–214, https://doi.org/10.1016/ j.msea.2013.04.079.

- [7] R. Chatterjee, J. Mukhopadhyay, A review of super plastic forming, Mater. Today Proc. 5 (2018) 4452–4459, https://doi.org/10.1016/j.matpr.2017.12.014.
- [8] S.P. Akula, M. Ojha, K.L. Rao, A.K. Gupta, A review on superplastic forming of Ti-6Al-4V and other titanium alloys, mater, Today Commun. 34 (2023) 105343, https://doi.org/10.1016/j.mtcomm.2023.105343.
- [9] E.-L. Odenberger, Concepts for Hot Sheet Metal Forming of Titanium Alloys, Department of Applied Physics and Mechanical Engineering, Division of Solid Mechanics, Luleå University of Technology, Luleå, 2009.
- [10] M. Kopec, K. Wang, D.J. Politis, Y. Wang, L. Wang, J. Lin, Formability and microstructure evolution mechanisms of Ti6Al4V alloy during a novel hot stamping process, Mater. Sci. Eng. A 719 (2018) 72–81, https://doi.org/10.1016/j. msea.2018.02.038.
- [11] G.A. Salishchev, R.M. Galeyev, O.R. Valiakhmetov, R.V. Safiullin, R.Y. Lutfullin, O. N. Senkov, F.H. Froes, O.A. Kaibyshev, Development of Ti–6Al–4V sheet with low temperature superplastic properties, J. Mater. Process. Technol. 116 (2001) 265–268, https://doi.org/10.1016/S0924-0136(01)01037-8.
- [12] T.B. Britton, F.P.E. Dunne, A.J. Wilkinson, On the mechanistic basis of deformation at the microscale in hexagonal close-packed metals, Proc. R. Soc. Math. Phys. Eng. Sci. 471 (2015) 20140881, https://doi.org/10.1098/rspa.2014.0881.
- [13] H.S. Chen, L.H. Du, M.S. Khan, T. Zhang, Y.H. Mu, Y. Zhang, Y. Li, A unified model to predict the hot stamping and subsequent stress-relaxation process of a Ti-6Al-4V alloy, IOP Conf. Ser. Mater. Sci. Eng. 1270 (2022) 012098, https://doi.org/ 10.1088/1757-899X/1270/1/012098.
- [14] Y. Zong, P. Liu, B. Guo, D. Shan, Springback evaluation in hot v-bending of Ti-6Al-4V alloy sheets, Int. J. Adv. Manuf. Technol. 76 (2015) 577–585, https://doi.org/10.1007/s00170-014-6190-z.
- [15] E.-L. Odenberger, R. Pederson, M. Oldenburg, Thermo-mechanical material response and hot sheet metal forming of Ti-6242, Mater. Sci. Eng. A 489 (2008) 158–168, https://doi.org/10.1016/j.msea.2007.12.047.
- [16] X. Liu, M. Kopec, O. El Fakir, H. Qu, Y. Wang, L. Wang, Z. Li, Characterisation of the interfacial heat transfer coefficient in hot stamping of titanium alloys, Int. Commun. Heat Mass Tran. 113 (2020) 104535, https://doi.org/10.1016/j. icheatmasstransfer.2020.104535.
- [17] Z. Hamedon, K.-I. Mori, T. Maeno, Y. Yamashita, Hot stamping of titanium alloy sheet using resistance heating. Вестник Магнитогорского Государственного Технического Университета ИМ ГИ Носова, 2013, pp. 12–15.
- [18] F. Ozturk, R.E. Ece, N. Polat, A. Koksal, Assessment of electrical resistance heating for hot formability of Ti-6Al-4V alloy sheet, Key Eng. Mater. 473 (2011) 130–136. https://doi.org/10.4028/www.scientific.net/KEM.473.130.
- [19] F. Ozturk, R.E. Ece, N. Polat, A. Koksal, Z. Evis, J.Y. Sheikh-Ahmad, Application of electric resistance heating method on titanium hot forming at industrial scale, Arabian J. Sci. Eng. 41 (2016) 4441–4448, https://doi.org/10.1007/s13369-016-21506
- [20] A.A. Camberg, A. Andreiev, S. Pramanik, K.-P. Hoyer, T. Tröster, M. Schaper, Strength enhancement of AlMg sheet metal parts by rapid heating and subsequent cold die stamping of severely cold-rolled blanks, Mater. Sci. Eng. A 831 (2022) 142312, https://doi.org/10.1016/j.msea.2021.142312.
- [21] F. Pfeifer, A. Dietrich, T. Marten, T. Tröster, B. Nacke, Investigation on inductive heating of sheet metal for an industrial hot stamping process, in: Hot Sheet Met. Form. High-Perform. Steel Proc. CHS2 7th Int, . Conf. Luleå Swed., 2019, pp. 2–5.
- [22] T. Marten, Erweiterung Des Portfolios Presshärtbarer Stähle Durch Gezielte Werkstoff-und Prozessmodifikationen, Shaker Verlag, 2017.
- [23] N. Pfeffer, S.N. Jäger, M.A. Kaiser, T. Meyer, A. Stark, H.W. Höppel, Enhancing mechanical strength of Ti-6Al-4V sheet material by short-time sub-β-transus solution heat treatment and additional short-time annealing, Mater. Sci. Eng. A (2025) 147787, https://doi.org/10.1016/j.msea.2025.147787.
- [24] Y. Chong, T. Bhattacharjee, M.-H. Park, A. Shibata, N. Tsuji, Factors determining room temperature mechanical properties of bimodal microstructures in Ti-6Al-4V alloy, Mater. Sci. Eng. A 730 (2018) 217–222, https://doi.org/10.1016/j. msea.2018.06.019.
- [25] Y. Chong, T. Bhattacharjee, Y. Tian, A. Shibata, N. Tsuji, Deformation mechanism of bimodal microstructure in Ti-6Al-4V alloy: the effects of intercritical annealing temperature and constituent hardness, J. Mater. Sci. Technol. 71 (2021) 138–151, https://doi.org/10.1016/j.jmst.2022.08.057.
- [26] C. de Formanoir, A. Brulard, S. Vivès, G. Martin, F. Prima, S. Michotte, E. Rivière, A. Dolimont, S. Godet, A strategy to improve the work-hardening behavior of Ti–6Al–4V parts produced by additive manufacturing, Mater. Res. Lett. 5 (2017) 201–208, https://doi.org/10.1080/21663831.2016.1245681.
- [27] O. Dumas, L. Malet, B. Hary, F. Prima, S. Godet, Crystallography and reorientation mechanism upon deformation in the martensite of an α-α' Ti-6Al-4V dual-phase microstructure exhibiting high work-hardening rate, Acta Mater. 205 (2021) 116530, https://doi.org/10.1016/j.actamat.2020.116530.

- [28] G.V.K. Jumov, Martensite crystal lattice, mechanism of austenite-martensite transformation and behavior of carbon atoms in martensite, Metall. Trans. A 7 (1976) 999–1011, https://doi.org/10.1007/BF02644066.
- [29] D. Liedtke, Über den Zusammenhang zwischen dem Kohlenstoffgehalt in Stählen und der Härte des Martensits, Mater. Werkst. 34 (2003) 86–92, https://doi.org/ 10.1002/mawe.200390022.
- [30] V.A. Lobodyuk, YuYa Meshkov, E.V. Pereloma, On tetragonality of the martensite crystal lattice in steels, Metall. Mater. Trans. A 50 (2019) 97–103, https://doi.org/ 10.1007/s11661-018-4999-z.
- [31] P.J. Fopiano, C.F. Hickey Jr., Strengthening Mechanisms During the Heat Treatment of Three Titanium Alloys-Ti-6al-4v, Ti-6al-6v-2sn, and Ti-8al-1molv, A. MATERIALS, M.R.C.W. MA, CFSTI, 1968.
- [32] T. Morita, K. Hatsuoka, T. Iizuka, K. Kawasaki, Strengthening of Ti-6Al-4V alloy by short-time duplex heat treatment, Mater. Trans. 46 (2005) 1681–1686, https://doi. org/10.2320/matertrans.46.1681.
- [33] S. Tanaka, T. Morita, K. Shinoda, Effects of short-time duplex heat treatment on microstructure and fatigue strength of Ti-6Al-4V alloy, in: 13th Int. Conf. Fract., 2013.
- [34] O. Dumas, L. Malet, G. Martin, P. Kwasniak, F. Prima, S. Godet, Exploring the strength-ductility space of Ti-6Al-4V through a quenching and partitioning approach, Mater. Sci. Eng. A 925 (2025) 147859, https://doi.org/10.1016/j. msea 2025 147859
- [35] ANSYS: LS-DYNA Keyword User's Manual R15.0: Volume vol. I, (2024). https://lsdyna.ansys.com/manuals/(accessed April 15, 2025).
- [36] M.A. Kaiser, F. Höschen, N. Pfeffer, M. Merten, T. Meyer, T. Marten, P. Rockicki, H. W. Höppel, T. Tröster, The new TISTRAQ process: solution treatment with rapid quenching and annealing for Ti-6Al-4V sheet metal part forming-investigation on heat transfer coefficient and influence on cooling rates, in: Mach Join (Ed.), Proc. 15th World Conf. Titan. Edinb. 2023 Chapter 14 Form, IOM3 Ti-2023 UK Sci. Comm., 2024.
- [37] N. Pfeffer, M.A. Kaiser, T. Meyer, M. Göken, H.W. Höppel, The new TISTRAQ process: solution treatment with rapid quenching and annealing for Ti-6Al-4V sheet metal part forming-the effect of processing parameters on microstructure and mechanical properties, in: Proc. 15th World Conf. Titan. Edinb. 2023 Chapter 14 Form. Mach. Join, IOM3 Ti-2023 UK Sci. Comm, 2024.
- [38] JMatPro: practical software for material properties. https://www.sentesoftware.co. uk/jmatpro/full-details, 2025. (Accessed 15 April 2025).
- [39] Verein Deutscher Ingenieure, VDI-Wärmeatlas, 11, Bearb. Und Erw. Aufl, Springer Vieweg, Berlin, Heidelberg, 2013, https://doi.org/10.1007/978-3-642-19981-3.
- [40] A, in: NSYS: L5-DYNA Keyword User's Manual R15.0, vol. III, 2024. https://lsdyna.ansys.com/manuals/. (Accessed 15 April 2025).
- [41] N. Demazel, H. Laurent, M. Carin, P. Le Masson, H. Salmon-Legagneur, A direct resistance heating method for shaped blank, J. Manuf. Process. 62 (2021) 772–783, https://doi.org/10.1016/j.jmapro.2020.12.056.
- [42] T. Maeno, K. Mori, T. Ogihara, T. Fujita, Blanking immediately after heating and ultrasonic cleaning for compact hot-stamping systems using rapid resistance heating, Int. J. Adv. Manuf. Technol. 97 (2018) 3827–3837, https://doi.org/ 10.1007/s00170-018-2232-2
- [43] T. Maeno, Y. Yamashita, K.-I. Mori, Hot stamping of titanium alloy sheets into U shape with concave bottom and joggle using resistance heating, Key Eng. Mater. 716 (2016) 915–922. https://doi.org/10.4028/www.scientific.net/KEM.716.915.
- [44] M.A. Kaiser, A. Reitz, S. Konrad, T. Meyer, T. Marten, T. Tröster, Untersuchung energieeffizienter und serientauglicher Erwärmungsstrategien mittels resistiver Erwärmung für den Prässhärteprozess, in: M. Merklein (Ed.), Proc. 18th Erlanger Workshop Warmblechumformung Erlangen 2023, 2023, pp. 99–118. Erlangen.
- [45] U. Zwicker, Titan Und Titanlegierungen, Softcover Reprint of the Hardcover, first ed., Springer, Berlin Heidelberg New York, 2014.
- [46] M. Bignon, E. Bertrand, P.E.J. Rivera-Díaz-del-Castillo, F. Tancret, Martensite formation in titanium alloys: crystallographic and compositional effects, J. Alloys Compd. 872 (2021) 159636, https://doi.org/10.1016/j.jallcom.2021.159636.
- [47] L. -c. Ming, M.H. Manghnani, K.W. Katahara, Phase transformations in the Ti-V system under high pressure up to 25 GPa, Acta Metall. 29 (1981) 479–485, https://doi.org/10.1016/0001-6160(81)90071-7.
- [48] J. Schindelin, I. Arganda-Carreras, E. Frise, V. Kaynig, M. Longair, T. Pietzsch, S. Preibisch, C. Rueden, S. Saalfeld, B. Schmid, J.-Y. Tinevez, D.J. White, V. Hartenstein, K. Eliceiri, P. Tomancak, A. Cardona, Fiji: an open-source platform for biological-image analysis, Nat. Methods 9 (2012) 676–682, https://doi.org/ 10.1038/nmeth.2019.
- [49] I. Arganda-Carreras, V. Kaynig, C. Rueden, K.W. Eliceiri, J. Schindelin, A. Cardona, H. Sebastian Seung, Trainable weka segmentation: a machine learning tool for microscopy pixel classification, Bioinformatics 33 (2017) 2424–2426, https://doi. org/10.1093/bioinformatics/btx180.